Ocean Engineering 288 (2023) 116001

Contents lists available at ScienceDirect

Ocean Engineering

journal homepage: www.elsevier.com/locate/oceaneng

An efficient method for unsteady hydrofoil simulations, based on Non-Linear Dynamic Lifting Line theory

John Martin Kleven Godø *, Sverre Steen

Norwegian University of Science and Technology, Department of Marine Technology, Jonsvannsveien 82, 7050 Trondheim, Norway

ARTICLE INFO

Keywords:
Hydrofoil
Fast ferry
Non-linear Dynamic Lifting Line
Vessel simulator
Seakeeping
Added resistance in waves

ABSTRACT

This paper presents a Non-linear Dynamic Lifting Line (NDLL)-based method for analysing hydrofoil vessels in waves. The method is validated, and its utility is demonstrated in a case study.

The NDLL accounts for dynamic and 3D effects through a panellized wake and allows the evaluation of the pressure distribution on hydrofoils. Improved models are presented for wake deformation, wake composition, hydrofoil interaction, and the viscous core of vortex wake models. Furthermore, an efficient way of accounting for Green function terms through a matrix interpolation method is presented.

Validation is performed by comparison with aerodynamic and hydrodynamic experiments and new 3D RANS simulations. The RANS simulations focus on geometries and operating conditions deemed representative of hydrofoiling fast ferries. Predictions of steady and dynamic lift, drag, wake velocities and cavitation inception are evaluated, and results correspond well with the benchmark data.

A simulator framework is introduced, which integrates the hydrodynamic model with kinetics, kinematics, and control system models. This enables analyses of free-running vessels under active control, including assessments of resistance, motions, and the hydrofoil pressure distribution.

The case study constitutes a qualitative verification of the simulator and flight control tuning methods, and reveals the possibility of negative added resistance in waves.

1. Introduction

Interest in hydrofoil technology has significantly increased over the past decade, with hydrofoils playing a vital role in various leisure craft designs and major sailing competitions. The fast ferry industry, driven by a growing focus on environmental impact, has once again embraced this technology. Hydrofoil fast ferries offer the potential for reduced resistance (Savitsky et al., 1984; Meyer and Wilkins, 1992), which can extend the range of zero-emission vessels, reduce the weight and cost of power systems, and decrease charging or refuelling requirements from shore. Additionally, hydrofoils improve seakeeping capabilities (Svenneby and Minsaas, 1992; Jorde, 1991; Meyer and Wilkins, 1992), enabling the use of smaller vessels in regions with challenging weather conditions.

In the early days of hydrofoil development, Ogilvie (1959) analysed hydrofoil vessels with linear quasi-static wing models, corrected for dynamic lift effects by the Theodorsen function (Theodorsen, 1935). While these models did not consider hydrofoil interaction or free surface effects, they provided valuable insights into hydrofoil seakeeping. A notable finding was the significant influence of dynamic lift effects, which reduced lift amplitudes by up to 40% compared to quasi-static equivalents at similar angles of attack. Subsequent studies by Keuning (1979) extended these methods to analyse surface-piercing hydrofoils, introducing non-linear equations of motion and variable hydrofoil area depending on submergence.

Frequency domain classical lifting line models have later been used in hydrofoil seakeeping analyses by Falch (1991a,b). The model was compared with experimental data, and good agreement was achieved at certain hydrofoil submergence conditions. Falch highlighted the fact that the linearized approach is less accurate in conditions where foils approach the water surface due to waves or vessel motion. Higher-fidelity Vortex Lattice Method (VLM) and Boundary Element Method (BEM) models were used by Feifel (1981) to analyse parts of the foil system for the Boeing 929 Jetfoil. These models demonstrated high accuracy in describing forces on individual hydrofoils, but the need for models accounting for hydrodynamic interaction, ventilation, and cavitation effects was emphasized. Important contributions were later made by Mørch (1992), analysing hydrofoil interaction with a lifting line model. A key finding from this work was that hydrofoil-generated gravity waves can lead to favourable inflow and reduced resistance of downstream hydrofoils.

* Corresponding author.
E-mail address: john.martin.godo@ntnu.no (J.M.K. Godø).

https://doi.org/10.1016/j.oceaneng.2023.116001
Received 27 March 2023; Received in revised form 22 August 2023; Accepted 7 October 2023

List of symbols

$\alpha_{ind,ij}$	Induced inflow angle on evaluation point i from vorticity at element j
$\boldsymbol{\delta}$	Vector of flap angle commands
$\boldsymbol{\eta}$	6-DOF NED position vector
$\boldsymbol{\nu}$	6-DOF BODY-frame velocity vector
$\boldsymbol{\tau_{FM}}$	6-DOF forces in BODY frame
$\boldsymbol{\tau}$	Control force, 6 DOF
$\boldsymbol{A}$	Linear equation system matrix used in the solution of $\boldsymbol{\Gamma}$ at each time step. $(N_L \times N_L)$
$\boldsymbol{b}$	Column vector used in the solution of the linear equation system for $\boldsymbol{\Gamma}$ at each time step. $(N_L \times 1)$
$\boldsymbol{C_{RB}}$	Coriolis-centripetal matrix, (6×6)
$\boldsymbol{dl}$	The vector from the start to the end of a vortex line segment
$\boldsymbol{F_{n_{AM}}}$	Added mass force
$\boldsymbol{K}$	Force coefficient matrix $(6 \times n_{controlinputs})$
$\boldsymbol{L_{FS,i}}$	Lift vector of line element i, based on a two-dimensional foil section lift model.
$\boldsymbol{L_{V,i,k}}$	Lift vector of line element i at time step k, based on a vortex model.
$\boldsymbol{M_{RB}}$	Rigid-body inertial matrix, (6×6)
$\boldsymbol{T}$	Control configuration matrix (6×6)
$\boldsymbol{T}^{\dagger}$	Moore–Penrose pseudo-inverse of $\boldsymbol{T}$
$\boldsymbol{u}$	Control input vector
$\boldsymbol{U}_{\Gamma,ij}$	Induced velocity on evaluation point i from vorticity at element j
δ_{vc}	Tuning parameter for viscous core radius in wake model
Λ	Aspect ratio
ϕ	Roll angle
θ	Pitch angle
θ_a	Pitch oscillation amplitude
ζ_a	Wave amplitude
c_i	Chord length of wing element number i.
C_P	$(p - p_\infty)/(1/2\rho U^2)$
C_r	Time averaged ratio of the area at a pressure below vapour pressure to the total wetted surface area
$C_{D,2D}$	2D drag coefficient
$C_{L,2D,f}$	2D lift coefficient due to flap deflection
$C_{L,2D}$	2D lift coefficient
$C_{L,\alpha}$	Lift coefficient per unit angle of attack
CG	Centre of gravity in the vessel-fixed reference frame. (3×1).
D	Net drag acting on the hydrofoil system in the vessel-bound coordinate frame
D_w	Resistance when operating in waves
D_{cw}	Resistance when operating in calm water
$f_{1,a}$	Flap oscillation amplitude, flap 1. Port side flaperon on the main hydrofoil.
$f_{2,a}$	Flap oscillation amplitude, flap 2. Starboard flaperon on the main hydrofoil.
$f_{3,a}$	Flap oscillation amplitude, flap 3. Elevator flap on tail hydrofoil.
L	Net lift acting on the hydrofoil system in the vessel-bound coordinate frame
M	Net moment acting on the hydrofoil system in the vessel-bound coordinate frame
N_L	The number of unknown vortex strengths at each time step.
Re_e	Effective Reynolds number. Defined as the Reynolds number for which a nonturbulent flow would yield the same drag coefficient on a sphere, as that found in the turbulent flow in question (Jacobs and Clay, 1936)
z_a	Heave oscillation amplitude

Dynamic modelling of hydrofoil vessels was significantly advanced by the work of van Walree (1999), who studied vessel behaviour in waves using a dynamic VLM code coupled with control system algorithms. This study included investigations of the interaction between hulls and foils during the take-off phase and incorporated Green functions for modelling the free surface, providing accurate predictions of gravity wave effects for engineering purposes.

Experimental work has traditionally played a crucial role in hydrofoil development. Extensive model testing in towing tanks, wind tunnels, and cavitation tunnels, as well as sea trials with free-running models, have been instrumental in the development of hydrofoil vessels such as the Kværner Fjellstrand FoilCat and Westamarin FoilCat 2900 (Jorde, 1991; Svenneby and Minsaas, 1992; Minsaas, 1993). Simulation models of the Mitsubishi Super-Shuttle 400 hydrofoil fast ferry by Toki et al. (1993) and Kihara et al. (1993) also appear to have made extensive use of model test data. Additionally, the work of van Walree et al. (1991) indicates that hydrodynamic models of the Rodriques Cantieri Navali hydrofoil vessels were built on a combination of lifting line theory and experimental data.

In recent years, many hydrofoil studies have focused on the modelling of foiling sailing yachts. The developed models are typically used in physical simulators for crew training and employ hydrofoil models that calculate forces based on two-dimensional (2D) lift and drag coefficients with correction factors for finite span effects (Rocchini and Conti, 2014; Findlay and Turnock, 2008a,b). However, these models often have limitations due to assumptions such as having a perfectly elliptic lift distribution and the neglect of foil interaction and gravity wave generation.

The versatility and accuracy of the lifting line theory, originally formulated by Prandtl (1918), was significantly increased by the introduction of a fully numerical approach to its solution by Phillips and Snyder (2000). This allows the simulation of wings of arbitrary shape and modelling of the interaction between sets of wings with a general mathematical formulation, for which the accuracy was shown to be comparable with inviscid CFD and panel methods. The method utilizes pre-generated 2D lift models for foil sections and matches the local solution for the sections with the outer flow conditions through an iterative numerical procedure. Graf et al. (2014) used a model of this type in the evaluation of forces on a wing sail, with 2D lift and drag models based on Reynolds-Averaged Navier–Stokes (RANS) simulations. Viscous drag and viscous effects on pressure drag are hence implicitly included. The correspondence with three-dimensional (3D) RANS was shown to be very good for both lift and drag up to angles approaching the stall angle. Duport et al. (2016) applied the theory on kite geometries with a curved dihedral shape and found it to give good correspondence with 3D RANS results. In a later study, Duport et al. (2017) investigated the accuracy for a kite geometry with a large skew angle, showing that global forces were relatively well captured while the spanwise distribution of lift deviated significantly close to mid-chord. A higher-order version of the approach of Phillips and Snyder (2000), with linearly varying vortex strength within line elements, was proposed by Hunsaker (2011). This did not improve on the order of convergence and required higher grid resolution for the same numerical accuracy. Steady-state numerical lifting line theory has been successfully applied in propeller design and analyses tools for marine

propellers and tidal turbines, including predictions of resistance to cavitation through interpolation of 2D profile pressure distributions (Epps et al., 2009; Epps, 2010; Epps et al., 2011; Epps and Kimball, 2013). Extensions to analyses of supercavitating hydrofoils have also been successfully created and shown to yield good correspondence with experiments and 3D RANS (Vernengo et al., 2017).

An unsteady non-linear lifting line code, building on many of the concepts of Phillips and Snyder (2000) for the line solution, was developed for wind turbine analyses by van Garrel (2003). In this context, "unsteady" means it can handle time-varying flow, including hysteresis effects on lift and drag. Furthermore, "non-linear" means it can handle non-linear relations between the angle of attack and profile lift and drag. Such nonlinearities can for instance be constituted by viscous separation effects present in the two-dimensional profile data used as input to the code. The code includes a vortex panel wake, capturing the three-dimensional induced velocity effects from both steady and unsteady lift. Experimental validation by Grasso et al. (2011) showed good agreement between simulations and model scale experiments on two wind turbine geometries. Marten et al. (2015) implemented a code building on the same theory, showing that efficiency could be increased by concentrating vortex elements in the far-field wake. The code gave results which matched experimental data well (Marten et al., 2016). It was later adapted for analyses of vertical axis wind turbines (Marten et al., 2018), which involve highly complex and dynamic flow physics where turbine blades experience large angles of attack, lift reversal and crossings through their own wakes. Results were compared with those of highly resolved RANS simulations, showing only minor deviations between the two (Balduzzi et al., 2018).

It is evident that modern numerical non-linear lifting line theory demonstrates great utility in many applications within aerodynamics and hydrodynamics. Since the wing model is simplified to a single line rather than a sheet of vortices or a set of surface panels, these methods will inherently be more numerically efficient than VLM or BEM codes. Furthermore, their independence of correction models for viscous effects on lift and drag also frees them from one of the major uncertainties associated with VLM or BEM models.

In this study, we have developed a new variety of the non-linear dynamic lifting line theory and investigated its accuracy in analysing hydrofoil fast ferries. Only vessels with fully submerged foil systems and no contact between hull and water are taken into consideration, since this is the typical design which is employed in contemporary conceptual vessels for the next generation of hydrofoil fast ferries (Candela, 2022; Artemis Technologies, 2022; Bieker Boats, 2022). Furthermore, we only consider the transit mode of operation, neglecting take-off, landing, and other operational modes in which the hull is in contact with water. Our code builds upon the theory presented by van Garrel (2003) and the codes of Kramer et al. (2018) and Godø et al. (2018), though incorporating a series of modifications. Free surface gravity waves are accounted for through a Green function model. Novel contributions have been made to the application of such, in the form of a matrix-based solution process, pre-calculation of influence functions and interpolation at run time, as well as its solution on a coarser subgrid and with a lower update rate than the remainder of the simulation. We also use the quasi-static version of Green functions in dynamic simulations, to speed up the solution process. A novel way of treating wake deformation is also presented, involving the deformation of only parts of the wake, accounting for only the most important induced velocity contributions and combining a dynamic and a quasi-static wake in a hybrid model. Contributions are also made to the simulation of hydrofoil interaction, in the form of a local-effects-focused model. A modification of a wake velocity smoothing function, or "viscous core" model, is also presented. Minor further additions relative to the cited NDLL codes are the inclusion of lift by virtual camber and added mass forces.

A pressure distribution model has been implemented, following a similar approach to that taken by Epps et al. (2011). Metrics are presented for the evaluation of various types of cavitation challenges for specific hydrofoil designs.

The presented combination of models and the extensions of theory, and its application to analyses of hydrofoil vessels, to the best knowledge of the authors, are novel contributions of current work.

To assess the accuracy of the proposed models, a comprehensive validation study is conducted for hydrofoiling fast ferries operating in both calm water and waves. This study evaluates the method's capability to predict steady and dynamic forces, the hydrofoil surface pressure distribution, hydrofoil interaction effects, and the inception of cavitation. The simulation results are compared with published experimental data as well as results from newly conducted 3D RANS simulations.

A simulator framework is presented, incorporating the hydrodynamic model in a six-degree-of-freedom (6-DOF) kinematics, kinetics, and control system simulator for marine vessels. This framework extends its scope beyond the analysis of predetermined-trajectory motion, allowing for the study of hydrofoil vessels operating in waves under active motion control. These coupled simulations capture the effects of control system action on hydrodynamic resistance, vessel motions, and the risk of cavitation.

In addition, a qualitative verification study is conducted to assess the performance of the complete model. This study involves simulating a free-flying hydrofoil vessel under active flight control, operating in both calm water and regular waves with varying encounter frequencies. The resulting vessel motions and flap actuation time histories are examined in terms of their physical sensibility and the effectiveness of the presented flight control system. Furthermore, the study investigates and discusses the frequency-dependent effects on added resistance and vessel motions in waves. This study inherently constitutes an assessment of whether the implemented methods for automatic control system tuning yield desirable vessel behaviour. It also presents valuable insights into vessel response and added resistance in waves for hydrofoiling fast ferries.

To facilitate further research, an open geometry model for hydrofoiling fast ferries is included in this work. This geometry is based on publicly available information regarding hydrofoiling passenger vessel concepts and is deemed representative of such designs. The design philosophy and resulting geometry are comprehensively presented, and the latter is made openly accessible through the companion website of the software mentioned in this paper (Godø and Steen, 2023). We hope that this resource will serve as a valuable starting point for future benchmarking studies.

The Non-linear Dynamic Lifting Line (NDLL) model and the simulator framework are implemented as part of the FASTSHIPS (Fast And Simple Tool for Simulation of HIgh Performance Ships) software package developed by the Department of Marine Technology at The Norwegian University of Science and Technology. The present work serves as a documentation of the theoretical aspects and validation of the code, contributing to its ongoing development and refinement

The text is organized into the following sections:

Section 2: Presentation of the NDLL-based hydrodynamic model.

Section 3: Validation of the NDLL model.

Section 4: Presentation of the closed-loop simulator framework.

Section 5: Case study.

2. NDLL for hydrofoils

The Non-linear Dynamic Lifting Line (NDLL) herein is heavily inspired by the work of van Garrel (2003), extended with the inclusions of free surface gravity waves, lift due to pitch rate, added mass forces, pressure distribution modelling, incoming waves, a more efficient wake and wake deformation model, a new viscous core model, and a different wing interaction model. Furthermore, the numerical solution algorithm for the equation system is modified.

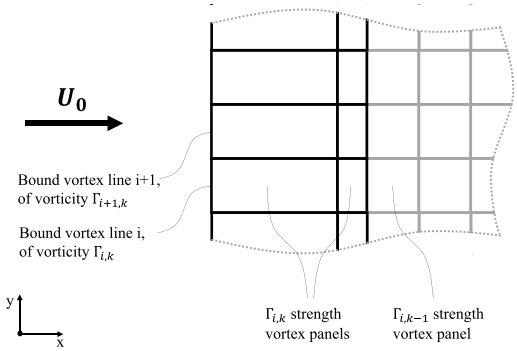

Fig. 1. An outer domain model as seen from above. Black lines are upstream vortex ring panels of equal vorticity strength to that of its corresponding bound line vortex. Grey lines are downstream vortex ring panels with vorticity equal to that of upstream panels at previous time steps. $\Gamma_{i,k}$ denotes the bound vortex strength of element i in the spanwise direction at time step k. The figure is truncated in the streamwise and spanwise directions.

A numerical lifting line works by connecting an outer three-dimensional potential flow solution with inner 2D lift models, the latter typically originating from RANS simulations. In the outer domain, the lifting surface is discretized as a set of line segments which act as vorticity generators. The generated vorticity is a function of the inflow angle, and the vorticity at each line segment affects the inflow angle on all other line segments. Through a known relation between the inflow angle and the generated vorticity, provided by 2D foil section lift models, the set of equations is closed and can be solved.

2.1. Inner and outer domains

In the current NDLL, the outer domain consists of a set of bound vorticity lines along the hydrofoil span, each followed by two vortex ring panels of equal strength to the bound line. The first panel extends from each end of the bound vortex line segment to the trailing edge of the wing/hydrofoil. The next goes from the trailing edge to a user-specified portion of a free convection trajectory between time steps. With N line elements, we have N vortex strength values constituting the unknowns at each solution step. Fig. 1 shows a top view of the outer domain, with the panels of unknown vortex strength marked by thick black lines. We denote the bound vorticity at element i at time step k as $\Gamma_{i,k}$. In the following presentation, we denote these upstream panels as $\Gamma_{i,k}$ panels.

Directly downstream of the $\Gamma_{i,k}$ panels follows a wake of vortex ring panels of strengths equal to that of the upstream panels at previous time steps. These are drawn in grey colour in Fig. 1. At each time step, the wing and $\Gamma_{i,k}$ panels move, and a new spanwise row of wake panels is created between the new position of the $\Gamma_{i,k}$ panels and the remainder of the wake. These have vortex strengths equal to those of the $\Gamma_{i,k}$ panels at the previous time step, indicated as $\Gamma_{i,k-1}$ in Fig. 1. The wake panels induce velocities on the bound vortex lines, hence accounting for the effects of steady-state downwash and time-varying lift. Furthermore, the wake deforms at each time step, as it is convected by induced velocities from itself and from the $\Gamma_{i,k}$ panels.

A two-dimensional lift model relates the local inflow angle to the generated vorticity at each element. The vorticity of each element affects the inflow to the element itself and to all other elements, yielding an implicit set of equations to be solved. The code allows the use of non-linear lift models and accounts for the effects of the streamwise induced velocities on the generated vorticity. It hence inherently yields a non-linear set of equations. This problem is solved through an iterative process of linearization and the solution of linear equation systems.

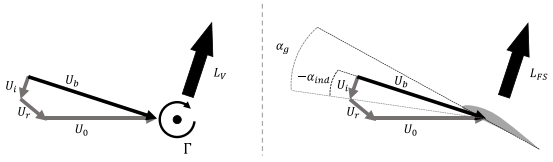

Fig. 2. The outer domain vortex lift model and the inner domain foil section lift model. The net inflow $\boldsymbol{U_b}$ consists of the undisturbed inflow from vessel motion $\boldsymbol{U_0}$, the inflow from waves and known parts of the wake $\boldsymbol{U_r}$, and the induced velocities from $\Gamma_{i,k}$ panels $\boldsymbol{U_i}$. Γ denotes the line vortex strength. $\boldsymbol{L_V}$ and $\boldsymbol{L_{FS}}$ are the lift vectors as calculated by the vortex model and the foil section lift model, respectively.

2.2. Solution algorithm

At each time step, the solution process starts with equating the lift of a line vortex model to the lift of a foil section lift model at each bound vortex line segment. Fig. 2 illustrates these two models. The balanced inflow vector $\boldsymbol{U_b}$ is the same for both models. $\boldsymbol{U_0}$ is the undisturbed inflow from vessel motion, $\boldsymbol{U_r}$ denotes all known disturbances from waves and wake history effects, and $\boldsymbol{U_i}$ denotes the unknown induced velocity connected with vortex strength at the current time step. $\boldsymbol{U_b}$ is hence a net local inflow vector, which is only known after solving the equation system at the current time step. All flow vectors are decomposed into a plane which is normal to the bound vortex segment, and all velocities are evaluated at the mid-point of these segments. $\boldsymbol{L_V}$ denotes the lift by the vortex model, Γ denotes the circulation strength, and $\boldsymbol{L_{FS}}$ denotes the lift by the two-dimensional foil section lift model. The inflow angles α_g and α_{ind} will be defined below.

The unsteady lift from a vortex segment exposed to the inflow vector $\boldsymbol{U}$ can be calculated by Eq. (1) (Katz and Plotkin, 2001). Γ denotes the vortex strength, c_i the chord length, $\boldsymbol{U}$ the inflow velocity, and $\boldsymbol{dl}$ the vector from the start to the end of the vortex line segment. Bold fonts are used for vectors. By applying backwards differencing and expressing the lift in the direction normal to the inflow on element i, $U_{b,i}$, we can express the lift per unit vorticity of element i at time step k by Eq. (2). Δt is the discrete time step size.

$$\boldsymbol{dL_i} = \rho(\Gamma_i + \frac{\delta\Gamma_i}{\delta t}\frac{c_i}{|\boldsymbol{U}\times\boldsymbol{dl_i}|})(\boldsymbol{U}\times\boldsymbol{dl}) \tag{1}$$

$$|\boldsymbol{L_{V,i,k}}| = \rho\left(\Gamma_{i,k} + \frac{\Gamma_{i,k}-\Gamma_{i,k-1}}{\Delta t}\frac{c_i}{|\boldsymbol{U_{b,i}}||\boldsymbol{dl_i}|}\right)|\boldsymbol{U_{b,i}}||\boldsymbol{dl}| \tag{2}$$

The two-dimensional foil section lift models are based on linear interpolation in a dataset of results from 2D RANS simulations. The dataset spans a range of angles of attack (α), flap angles (δ), camber heights (h_c), thickness ratios (t_c), and Reynolds numbers (Re). A correction for virtual camber due to pitch rate is added (Leishman, 2006), resulting in Eq. (3) for the lift in the normal direction to the inflow vector $\boldsymbol{U_b}$. c, $\dot{\theta}$, and $C_L(\alpha,\delta,h_c,t_c,Re)$ denote the chord length, pitch rate, and the steady-state lift coefficient, respectively.

$$|\boldsymbol{L_{FS,i}}| = \frac{1}{2}\rho|\boldsymbol{U_b}|^2\left(C_L(\alpha,\delta,h_c,t_c,Re) + \frac{\pi c\dot{\theta}}{|\boldsymbol{U_b}|}\right) \tag{3}$$

The Biot–Savart law is used for relating the inflow direction to the unknown vortex strengths. This was formulated numerically without a singularity by Phillips and Snyder (2000), and is here presented as Eq. (4). $\boldsymbol{r}_{1,ij}$ and $\boldsymbol{r}_{2,ij}$ denote the vectors from each end of vortex element j to the evaluation point of element i, Γ_j denotes the vorticity of element j, and $\boldsymbol{U}_{\Gamma,ij}$ denotes the induced velocity vector on element i from element j.

$$\boldsymbol{U}_{\Gamma,ij} = \frac{\Gamma_j}{4\pi}\frac{(|\boldsymbol{r}_{1,ij}|+|\boldsymbol{r}_{2,ij}|)(\boldsymbol{r}_{1,ij}\times\boldsymbol{r}_{2,ij})}{|\boldsymbol{r}_{1,ij}||\boldsymbol{r}_{2,ij}|(|\boldsymbol{r}_{1,ij}||\boldsymbol{r}_{2,ij}|+\boldsymbol{r}_{1,ij}\cdot\boldsymbol{r}_{2,ij})} \tag{4}$$

The induced angle of attack on element i per unit vorticity of element j can now be expressed by Eq. (5). $\boldsymbol{u}_{n,i}$ and $\boldsymbol{u}_{t,i}$ are the normal and

tangential vectors of the foil section chord of element i, respectively. The equation assumes small angles, so that $\tan\alpha \approx \alpha$.

$$\alpha_{ind,ij} = \frac{\boldsymbol{U}_{\Gamma,ij} \cdot \boldsymbol{u}_{n,i}}{\Gamma_j(\boldsymbol{U}_{b,i} \cdot \boldsymbol{u}_{t,i})} \tag{5}$$

Linearizing the non-linear lift model for $C_L(\alpha, \delta, h_c, t_c, Re)$ about the relevant angle of attack and combining it with the influence factors for inflow angles, we can express the lift on element i by Eq. (6). $\alpha_{g,i}$ denotes the gross inflow angle to element i without accounting for induced velocities by $\Gamma_{i,k}$ elements. N_L, $\dot{\theta}_i$, and $C_{L_0,i}$ denote the set of bound vortex elements, the local pitch rate of line element i, and the lift coefficient as found by the linearized lift model of element i at $\alpha = 0$, respectively. The slope of the linearized lift model at element i is denoted $\frac{\delta C_{L,i}}{\delta\alpha}$.

$$L_{FS_i} = \frac{1}{2}\rho|\boldsymbol{U}_{b_i}|^2\left(C_{L_0,i} + \frac{\delta C_{L_i}}{\delta\alpha}\left(\alpha_{g_i} + \sum_{j\ in\ N_L}\alpha_{ind,ij}\Gamma_j\right) + \frac{\pi c_i\dot{\theta}_i}{|\boldsymbol{U}_{b_i}|}\right) \tag{6}$$

An equation system is built by equating Eqs. (2) and (6) for each bound vortex element. Except for the unknown $\boldsymbol{U_b}$ vector in Eq. (6), we now have a set of N_L linearized equations for the N_L unknown vortex strengths, which can be expressed on the form $\boldsymbol{A\Gamma} = \boldsymbol{b}$. $\boldsymbol{\Gamma}$ denotes a vector of all the unknown bound vortex strengths. This set of equations can be solved with standard linear equation solvers. $\boldsymbol{U_{b,i}}$ is the vectorial sum of $\boldsymbol{U_0}$, $\boldsymbol{U_r}$, and $\boldsymbol{U_i}$. $\boldsymbol{U_0}$ is found for each spanwise element from the instantaneous vessel velocity in six degrees of freedom (DOF). $\boldsymbol{U_r}$ is calculated from the sum of the inflow from waves and the induced velocities from the known parts of the wake. Note that the latter does not include the bound line and the upstream $\Gamma_{i,k}$ elements. At the first time step, we close the equation system by setting $\Gamma_{i,k-1} = \Gamma_{i,k}$ and running the first solution iteration with $\boldsymbol{U_b} = \boldsymbol{U_0} + \boldsymbol{U_r}$. In later iterations, we use $\boldsymbol{U_i}$ from the previous solution iteration to construct $\boldsymbol{U_b}$. For each time step, we conduct an iterative loop where we construct the linear equation system, solve it, update $\boldsymbol{U_b}$, linearize lift models about their new operating point, and repeat. Iteration is terminated when the difference between two consecutive solutions of $\boldsymbol{\Gamma}$ is below a given threshold. In the first iteration of a new time step, we assume $\boldsymbol{U_i}$ to be equal to that of the last iteration of the previous time step.

2.3. Force evaluation

When the solution algorithm has converged, the inflow to every line element is known. We now calculate the forces acting on each element from the two-dimensional lift and drag models. The circulatory lift is calculated by Eq. (6), and foil section drag is found from drag models based on interpolation in the same RANS data set as used for creating the lift models. The added mass force is approximated as a chord-normal force described by Eq. (7), modified from Leishman (2006) and Newman (1977). $\boldsymbol{F}_{n_{AM}}$ and x_{rot} denote the added mass force vector and the chordwise relative centre of rotation as measured from the leading edge, respectively. The total force on each line segment is found by summing force vectors from the circulatory lift, the section drag, and the added mass forces.

$$\boldsymbol{F}_{\boldsymbol{n_{AM}}} = \frac{\pi c_i^2}{4}\left(\frac{\delta(\boldsymbol{U_b}\cdot\boldsymbol{u_n})}{\delta t} + (\boldsymbol{U_b}\cdot\boldsymbol{u_t})\dot{\theta} + (0.75 - x_{rot})c_i\ddot{\theta}\right)|\boldsymbol{dl}|\boldsymbol{u_n} \tag{7}$$

2.4. Two-dimensional foil section models

The NDLL can take two-dimensional (2D) lift and drag models from various sources as input. In the current work, we use models created from two sources: XFOIL and 2D RANS simulations. Both are based on simulations of geometries and operating conditions between which the angle of attack, flap angle, camber ratio, thickness ratio, and Reynolds number were varied. $C_L(\alpha, \delta, h_c, t_c, Re)$, $\frac{\delta C_L}{\delta\alpha}(\alpha, \delta, h_c, t_c, Re)$, and $C_D(\alpha, \delta, h_c, t_c, Re)$ are found by linear interpolation in the dataset. To speed up the interpolation process at run time, a pre-processing step is performed, in which sub-models for sections of constant camber and thickness are created for each line element of the hydrofoil. Furthermore, interpolation models for the pressure distribution on the foil section surfaces are created from the same dataset. At run time, these can be used for finding the three-dimensional (3D) pressure distribution and predicting the inception of cavitation. This is detailed in Section 2.7. The two-dimensional RANS simulations used in the foil section force and pressure models used herein were performed as single-phase steady simulations in OpenFOAM. Details of the setup are given in Appendix A.

2.5. Wake model

Wake panels constitute a key part of a dynamic lifting line, storing streamwise and spanwise wake vorticity, hence affecting the inflow to the bound line elements. The calculation of the induced velocities from the wake and its potential deformation constitutes a major part of the numerical load of running the code. The following sections present the main characteristics of the wake model of the presented simulation method and highlight a set of measures which have been taken to increase its numerical efficiency.

2.5.1. Viscous core

The induced velocities from the wake are calculated by Eq. (4). This has a singularity when the distance between the evaluation point and vortex approaches zero. Since we are simulating full hydrofoil systems where the wake of an upstream hydrofoil might directly intersect downstream hydrofoils, we must eliminate this singularity to achieve stable simulations. This is typically done by the introduction of a so-called viscous core model for the vortex lines, forcing the induced velocities towards zero when the distance between the line and the evaluation point approaches zero.

A linear velocity ramp-down was applied by van Walree (1999), while a smooth weighting function was introduced by van Garrel (2003) through the introduction of an extra term δl_0 in the denominator of Eq. (4). l_0 denotes line element length and δ is a tuning parameter. This model is numerically efficient and provides stable simulations, but has the disadvantage of decreasing the radius of the affected zone with increased simulation resolution. We have observed that this leads to spanwise oscillating inflow predictions for downstream hydrofoils in cases with fine spanwise resolution and coarse time steps. This leads to unrealistic predictions of the inception of cavitation. The disadvantage of a correlation between the element length and the viscous core radius was pointed out by Marten et al. (2016), who solved the problem by introducing a two-parameter time-dependent model for the radius. This does however require tuning of two parameters.

We suggest a different approach to overcome the challenges of the model of van Garrel (2003). Instead of using the element length as part of the new denominator term, we use the element spacing s_0. For spanwise vortex lines, we set $s_0 = |U\Delta T|$, where U denotes the instantaneous forward speed and ΔT denotes the instantaneous time step. For streamwise vortex lines, we set s_0 equal to the spacing of the spanwise bound vortex control points at the corresponding spanwise position. This model introduces a smoothing of the induced velocity as long as the distance between an evaluation point and a singularity element is in the order of the distance between the singularity elements. This means the influence of the smoothing function will be felt at an evaluation point placed in between two singularity elements, but not for one which is significantly further away from the singularity elements. The modified Biot–Savart equation is shown in Eq. (8). δ_{vc} acts as a tuning parameter and is typically set in the range of $0.2 < \delta_{vc} < 1.0$.

$$\boldsymbol{U}_\Gamma = \frac{\Gamma}{4\pi}\frac{(r_1 + r_2)(\boldsymbol{r_1}\times\boldsymbol{r_2})}{r_1 r_2(r_1 r_2 + \boldsymbol{r_1}\cdot\boldsymbol{r_2}) + (\delta_{vc}s_0)^2} \tag{8}$$

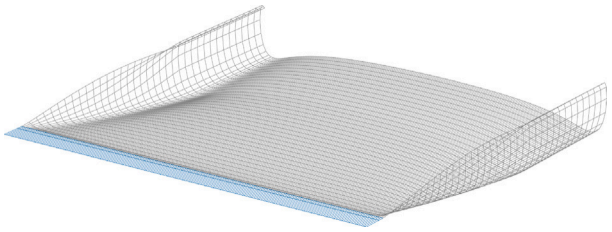

Fig. 3. Wake shape as calculated with the presented method of wake deformation. The foil section chord lines, which are not part of the simulation, are sketched in blue for illustration purposes. Wake vortex lines are shown in grey colour.

2.5.2. Wake deformation

van Walree (1999) investigated the importance of wake deformation on hydrofoil forces predicted by his VLM code. He found that this had virtually no influence on either steady or unsteady forces on single-hydrofoil simulations. However, both the overall wavy shape of the wake and wake roll-up affected the forces on downstream hydrofoils in unsteady multi-hydrofoil simulations of certain wavelengths. Although not specifically investigated by van Walree, it might be reasonable to believe that the wake shape has an effect on the oscillatory angle of attack amplitudes of downstream hydrofoils, and hence on predictions of the inception of cavitation when operating in waves.

We suggest a new and numerically efficient approach to wake deformation. In this, we only deform the upstream section of the wake, typically limited to 5–15 chord lengths from the hydrofoil. Furthermore, to limit the computational load we only account for the influence of the following parts of the domain on wake deformation:

- Bound vortex lines
- Trailing vortex lines of the $\Gamma_{i,k}$ panels
- Trailing vortex lines in the wake, within the deformation region.
- In free surface cases: Reversed-vorticity mirror sources of the above.

Several effects are neglected, implicitly assuming negligible effects on wake deformation. This includes the induced velocities from the spanwise wake vortex lines, from vortex lines downstream of the deformation region, Green function terms of the velocity potential, and induced velocities from waves.

This approach to wake deformation seems not to have been investigated in published literature. It originates from a hypothesis that the most important effect of wake deformation on foil interaction is that of the wake being convected downwards in the near-field wake of the hydrofoil. Hydrofoil vessels typically have all hydrofoils in the same horizontal plane, to reduce the risk of ventilation while keeping within draft restrictions. A minor vertical convection of the wake might hence have significant effects on the induced velocities on downstream hydrofoils, as it alters the wake trajectory into a path underneath rather than straight onto the latter. It is judged likely that this downwards convection effect is mainly induced by the bound vortex line, and that it is hence strongest in the near-wing wake. Accounting for wake deformation only in this region might be a reasonable compromise between accuracy and computational load.

Each wake vertex is deformed by induced velocities as calculated midway between the vertex and the next vertex downstream. An example of a deformed wake following the described approach is shown in Fig. 3. In the figure, the wake has a total length of 30 chord lengths and is deformed through a region extending 20 chord lengths downstream of the hydrofoil. For illustration purposes, the vertical axis is scaled differently than the horizontal axes. The simulated case is an aspect-ratio 10 rectangular hydrofoil of NACA66-010 + NACA a = 0.8(mod) profile of relative camber height 0.02, operating in infinite fluid.

2.5.3. Hybrid steady/dynamic wake

As a measure to increase computational efficiency, we have implemented an approach of stretching the most downstream wake elements of the simulation to a far downstream position, typically to a total streamwise wake length of 100 chord lengths. This means that the wake will be fully dynamic and potentially deforming in the upstream section, while the downstream region is constituted by a quasi-steady wake of long streamwise vortex lines. With this approach, we can truncate the non-stretched part of the wake far more upstream than what would otherwise be possible without losing significant accuracy.

The method of stretching the downstream section of the wake is particularly useful in combination with the wake deformation method presented above. Combining the two methods, we create a two-part wake where the upstream section is fully dynamic and deforming, while the downstream section is a quasi-static streamwise extrusion of the downstream row of dynamic wake elements. This approach is highly beneficial in foil interaction cases with small or no dynamic lift effects. In these cases, a conventional deforming panellized wake would be numerically demanding, since it would necessarily have to stretch from the upstream hydrofoil to a distance downstream of the downstream hydrofoil. This would yield a very large number of wake panels on and from which to calculate interaction effects. Truncating the wake deformation and streamwise resolution at a relatively short distance from the upstream hydrofoil captures the main effect of wake deformation without requiring nearly as many wake panels or interaction paths. The stretched downstream section of the wake ensures that the main effects of hydrofoil interaction can be calculated. Since no spanwise vortex lines are present in the stretched part of the wake, this approach is not suitable for evaluating hydrofoil interaction in highly dynamic cases.

2.6. Interaction model

Foil interaction is handled by accounting only for the effect of upstream hydrofoils on downstream hydrofoils. Different hydrofoils comprising a hydrofoil system are simulated in independent domains, and induced velocities from the upstream hydrofoils are introduced as external disturbances on the downstream hydrofoils. This halves the computational load originating from the calculation of interaction effects, relative to a two-way coupling, when simulating a two-hydrofoil system.

To further improve the numerical efficiency, we limit the region in which the wake vorticity affects a downstream hydrofoil between upstream and downstream thresholds. These are typically set to 5–8 chord lengths from the downstream hydrofoil. This way the computational load of calculating the wake influence on a downstream hydrofoil is again approximately halved as compared to accounting for the effect of the whole wake. The main interaction effect is captured, since according to Eq. (4) the induced velocities are inversely proportional to the distance from the vorticity element, meaning the wake elements located far from the downstream hydrofoil make little impact on the net inflow to this.

2.7. Pressure distribution model

The developed code assumes that the hydrofoils operate within regimes where cavitation does not significantly affect hydrodynamic forces, equivalently to assumptions used in propeller design (Epps et al., 2009, 2011). This assumption allows for a decoupling of force and cavitation analyses, and might be justified by a claim that a hydrofoil which is significantly affected by cavitation should anyway be re-designed so that it is not.

To evaluate whether there is a risk of the inception of cavitation, we propose a simplified and numerically efficient model. Surface pressures are extracted from the set of 2D RANS simulations used to create lift and drag models. These are used to generate a dataset of distributions of the pressure coefficient $C_P = (p - p_\infty)/(0.5\rho U^2)$, as a function of α, δ,

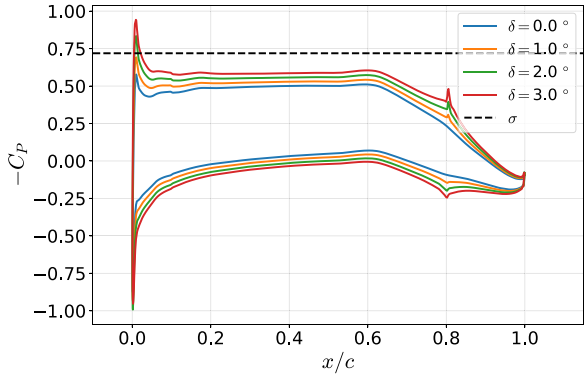

Fig. 4. Interpolated distributions of $-C_P$ from 2D model of a NACA 66, a = 0.8(mod) foil section at various flap angles. The cavitation number *sigma* for operation at 35 knots at 2 m submergence is indicated with a dashed black line.

h_c, t_c, and Re. p_∞ denotes the free-stream static pressure and p is the pressure at the foil surface. A linear interpolation model is then created, allowing the extraction of the distribution of C_P as a function of the mentioned parameters. By assuming that any point which falls below the cavitation number σ immediately leads to local cavitation, we can make a simplified cavitation assessment under the assumption that cavitation itself does not affect the pressure distribution. Furthermore, we can identify the location and hence estimate the type of cavitation.

Examples of extracted distributions of $-C_P$ from such an interpolation model are shown in Fig. 4. The model in question is for a NACA66, a = 0.8(mod) section of $t/c = 0.10$, $h_c = 0.02$, operating at $\alpha = 1°$ at various flap angles. σ, corresponding to 35 knots and 2 m submergence, is indicated with a dashed black line.

With this method, we get a cavitation assessment which includes the combined effects of flap angles, incoming waves, vessel orientation, vessel position, and vessel motion, allowing the extraction of statistical data on cavitation for hydrofoil vessels running in rough seas with active ride control. The method implicitly assumes the presence of cavitation not to affect the pressure distribution outside the cavitating region, since RANS simulations without cavitation modelling are used to find pressure distributions. No modifications have been made to these results to account for local cavitation regions. A natural extension of this approach would be to use 2D models from RANS simulations with cavitation modelling, as done in the steady lifting line by Vernengo et al. (2017). This is however outside the scope of current work.

We introduce a parameter for the combined quantification of the temporal and spatial extent of minor cavitation regions. This parameter is given in Eq. (9). $A_c(t)$ denotes the instantaneous foil area where $-C_P > \sigma$, A_w denotes the wetted foil area, and T_0 and T_{end} are the start and end times of the simulation, respectively. Consequently, C_r denotes the average relative area below vapour pressure during the simulation.

It is important to point out that this model only accounts for the pressure distribution in non-cavitating conditions. It does not involve modelling of cavitation itself. This means it should only be used to identify whether cavitation occurs, not to evaluate the extent of regions of significant cavitation. The introduced metric for the average cavitating area might still be useful, for instance for identifying the existence of local regions in which pressure temporarily drops below the vapour pressure during dynamic simulations.

$$C_r = \frac{\int_{t=T_0}^{T_{end}} A_c(t)dt}{A_w(T_{end} - T_0)} \tag{9}$$

2.8. Free surface model

One of the key differences between the current code and those used for wind turbine analyses by e.g. van Garrel (2003) and Marten et al. (2016) is the presence of a free surface. The way this is modelled has a significant influence on the numerical efficiency of the presented method and hence deserves some attention.

Kramer et al. (2018) found that it is sufficient to account for the free surface by reversed-sign mirroring of vorticity in analyses of single hydrofoils, hereby implicitly assuming an infinite submergence Froude number. This study was however limited to a narrow range of aspect ratios and relatively high values of submergence Froude numbers of 4 and 6. It did not account for interaction effects between foils.

Mørch (1992) investigated interaction effects between hydrofoils and found that gravity waves, which are not included in an infinite Froude number model, have a significant influence on induced velocities downstream of a hydrofoil. The effects on hydrofoil interaction are especially strong if the streamwise distance between hydrofoils is in the order of several span lengths, such as is typically found in canard hydrofoil systems. He also found that gravity waves might matter for single hydrofoils if the Froude number is sufficiently low.

van Walree (1999) evaluated the effects of gravity waves in seakeeping analyses. His results indicate that vessel motions are not significantly affected by gravity waves generated by the hydrofoils, while mean flap angles are. The latter affects cavitation and added resistance estimates. Van Walree theorized that the reason for the negligible effect on vessel motions might be that excitation and damping forces were similarly affected by the neglect of gravity waves, yielding a relatively small net effect on motions. Pressure distribution and added resistance were not investigated.

The current code is intended for analyses of full hydrofoil systems operating in a wide range of Froude numbers. Added resistance and assessments of the risk of cavitation are among the key results to be extracted. Based on the findings mentioned above, it is hence judged necessary to include a model of gravity wave effects. The implemented model is based on Green functions, meaning that the velocity potentials for the vortex lines in the outer solution are modified to satisfy a linear free surface condition. This can be implemented in steady or unsteady versions, the latter of which is significantly more computationally demanding. Both versions have been implemented in the current code, and the unsteady version was found to yield too high a computational load to allow it to be used in practical calculations. We have hence applied a steady-state free surface condition in all simulations, including unsteady cases. We only present the steady version here.

Mørch (1992) presents the velocity potential for a half-infinite horseshoe vortex line as in Eq. (10). β denotes dihedral angle, (x, y, z) are the coordinates of the evaluation point, and (ξ, η, ζ) the coordinates of the singularity. I_2 and I_3 are the parts of the velocity potential accounting for gravity waves, presented in Eqs. (12) and (13). v and u are defined in Eqs. (14) and (15). E_1 is the complex exponential integral and H is the Heaviside step function. $k_0 = g/U^2$. I_1, presented in Eq. (11), accounts for the direct effects of the lines and their mirror lines above the free surface. R_0 and R are the distances between the evaluation point and the singularity, and between the evaluation point and the mirror singularity, respectively.

$$\phi(x, y, z, \xi, \eta, \zeta) = Re\left\{\frac{1}{4\pi}\int_{-s}^{s}\Gamma\left[-\left(\frac{\delta I_1}{\delta\eta} + \frac{\delta I_2}{\delta\eta} + \frac{\delta I_3}{\delta\eta}\right)\sin\beta + \left(\frac{\delta I_1}{\delta\xi} + \frac{\delta I_2}{\delta\xi} + \frac{\delta I_3}{\delta\xi}\right)\cos\beta\right]ds\right\} \tag{10}$$

$$I_1 = \int_0^\infty \left(\frac{1}{R_0} - \frac{1}{R}\right)d\xi \tag{11}$$

$$I_2 = Re\left\{\frac{i2k_0}{\pi}\int_{-\pi/2}^{\pi/2}\cos\theta\int_0^\infty e^v E_1(v)d\xi d\theta\right\} \tag{12}$$

$$I_3 = Re\left\{ i4k_0 \int_{-\pi/2}^{\pi/2} \sec^2\theta \int_0^{\infty} H(k_0(x-\xi))e^u d\xi d\theta \right\} \tag{13}$$

$$\upsilon = k_0(z+\zeta)\cos^2\theta + k_0|y-\eta|\cos\theta\sin\theta + ik_0|x-\xi|\cos\theta \tag{14}$$

$$u = k_0(z+\zeta)\sec^2\theta + ik_0|y-\eta|\sec^2\theta\sin\theta + ik_0|x-\xi|\sec^2\theta \tag{15}$$

In the gravity wave model, we are interested in the induced velocities from the gravity part of the velocity potential, which can be found by differentiation of Eq. (10) with respect to y and z. As is evident from Eqs. (11), (12), and (13), the resulting expressions will contain integrals with respect to theta. Van Walree points out that this introduces two challenges: Singularities and highly oscillating integrands. The former originates from I_2 and to solve it, van Walree creates a series expansion for this term before finding spatial partial derivatives and integrating with respect to θ. We have employed a more straightforward engineering approach. It is recognized that the singularities of all I_2 derivatives are located at endpoints and the internal point $\theta = \arctan -\frac{z+\zeta}{|y-\eta|}$. Close to the latter, it goes to positive and negative infinite values. We evaluate the integral as two separate numerical integrals, with the closest evaluation points placed at equal distances on each side of the interior point singularity. To solve the challenge of highly oscillating integrands, which originates from the I_3 derivatives, we employ a trick proposed by Hally (1994). This involves a simple re-writing of the integration variable into $t = \tan\theta$. This significantly reduces the slope of the oscillatory parts of the integrand, allowing for less computationally demanding numerical integration with fewer integration points.

The last step in evaluating velocities from gravity waves is to perform an integration of the derivatives of Eq. (10) along the span of the wave-generating hydrofoil. We do this numerically and propose an efficiency-enhancing approach to this step. It is recognized that, if assuming small roll and pitch angles and evaluating the influence of gravity waves only from vessel-bound hydrofoils to vessel-bound evaluation points, the only varying parameters in any equations are U, the $(z+\zeta)$ terms of Eqs. (14) and (15) and the Γ values along the span of the wave generating hydrofoil. Everything else is only dependent on the vessel geometry and can be calculated in a pre-processing stage. In simulations where the speed and operating depth are close to constant, which is typically the case for steady-state transit of hydrofoil vessels, we simplify the Green function evaluations by assuming U, z, and ζ to be constant, leaving only Γ as the run time-varying parameter. Numerical evaluation of the integral then leaves us with the task of evaluating a sum of terms which are proportional to element vorticity, for each evaluation point. The potential function values originating from gravity waves at evaluation points can now be expressed as a matrix multiplication in the form of Eq. (16). ϕ is here an $N_{ev.p}$ vector of phi values at the evaluation points. $\boldsymbol{K}(z)$ is an $(N_{ev.p} \times N_{l.el.})$ matrix, where $N_{l.el.}$ denotes the number of line elements in the wave generating hydrofoil. Γ is a, $N_{l.el.}$ vector of vorticity strength of the bound line elements of the wave-generating hydrofoil. Each component of the induced velocities can now be expressed as in Eq. (17). $\boldsymbol{U}_k(z)$ is a vector of $N_{ev.p}$ induced velocity components along axis k and $\boldsymbol{Q}_k$ contains the spatial partial derivatives of the terms of $\boldsymbol{K}(z)$ in the k direction.

$$\boldsymbol{\phi} = \boldsymbol{K}(z)\Gamma \tag{16}$$

$$\boldsymbol{U}_k(z) = \boldsymbol{Q}_k\boldsymbol{\Gamma}, k = 2,3 \tag{17}$$

A further improvement of this approach is to calculate the $\boldsymbol{Q}_k(z)$ matrix for a set of combinations of U and z, and interpolating between these at run time. This allows the use of this matrix approach to the integration of gravity wave-induced velocities also in cases of non-constant velocity and vertical position. Since the dynamics of the speed and vertical position of the vessel are typically far slower than wake vortex dynamics, the interpolation between $\boldsymbol{Q}_k(z)$ matrices can be done at a significantly lower frequency than the NDLL updates. The numerical burden of including gravity waves in the calculation of induced velocities at all relevant evaluation points is now reduced to a matrix–vector multiplication at each time step, plus a set of $N_{ev.p} \times N_{elements}$ interpolations between matrix entries at a much lower update rate.

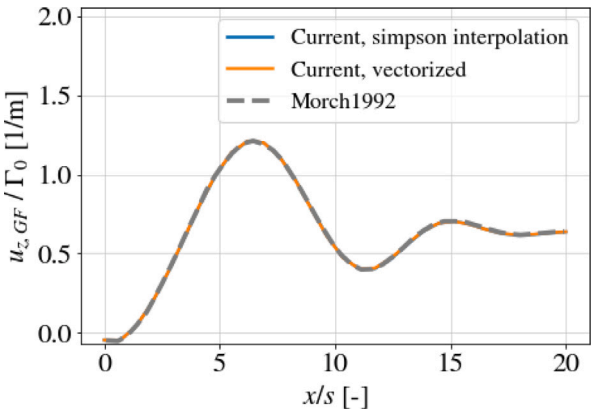

Fig. 5. Gravity wave-induced vertical velocity relative to hydrofoil vorticity, for an elliptically loaded hydrofoil operating at h/s = 0.2, Submergence Froude number 5.81. Results from Mørch (1992) are plotted together with current results using two different calculation approaches. $u_{z,GF}$ denotes vertical velocity component due to Green Function influence and Γ_0 denotes mid-span two-dimensional bound circulation of the hydrofoil.

Moving the calculation of Green function influence terms to the pre-processing stage yields efficient simulations at run time. For short simulations, it does however lead to a disproportionately long pre-processing time relative to simulation time. A further improvement of efficiency is therefore implemented, based on the insight that the spatial variation of gravity wave effects is small relative to the size of line elements. Methods for calculating influence functions accept a spatial downsampling parameter d. Line vertices and elements are then chosen with index spacing of d, before calculating influence functions. This means the influence functions for gravity waves are calculated on a coarser grid, where d neighbouring line elements are combined into one super-element between their extremity points. A transformation to a full influence matrix is thereafter performed, by assuming the influence from all elements within one super-element to have an influence function equal to that of the super-element divided by d, and by linear interpolation between evaluation points.

To make sure the gravity wave Green functions are implemented correctly, we have chosen to reproduce a result from Mørch (1992). He calculated the gravity wave-induced velocities along a streamwise line from midspan to a distance of 20 chord lengths downstream, for an elliptically loaded wing submerged 0.2 span lengths operating at submergence Froude number 5.81. The results of Mørch are plotted together with current results in Fig. 5. $u_{z,GF}$ denotes vertical velocity component due to Green Function influence and Γ_0 denotes mid-span two-dimensional bound circulation of the hydrofoil. The figure includes results of both direct integrations of derivatives of Eq. (10) and from the presented matrix multiplication approach. The results are practically identical.

A visual inspection of the vertical part of gravity wave-induced velocities in a horizontal plane is presented in Fig. 6, constituting a qualitative verification of the sensibility of the Green function implementation.

2.9. Overview of the NDLL model

Fig. 7 shows a flowchart of the Non-Linear Dynamic Lifting Line (NDLL) model, as executed for each time step of a dynamic simulation. The *inner solution loop* is repeated iteratively until Γ converges.

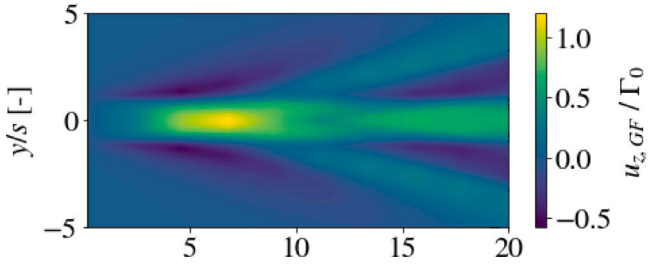

Fig. 6. Gravity wave-induced vertical velocity relative to hydrofoil vorticity for an elliptically loaded hydrofoil operating at h/s = 0.2 and a submergence Froude number of 5.81. $u_{z,GF}$ denotes the vertical velocity component due to Green Function influence and Γ_0 denotes the mid-span two-dimensional bound circulation of the hydrofoil.

Details of the inner solution loop and the symbols therein are given in Section 2.2. t, $\boldsymbol{\eta}$ and $\boldsymbol{\delta}$ denote the simulated time, the six degree of freedom position of the hydrofoil system in the global coordinate frame, and a vector of flap angles, respectively. Dots denote time derivatives. L, D, and M denote the net lift, drag, and moment acting on the hydrofoil system, about the set coordinate frame origin, respectively. A new time step is initiated by providing a new set of time, position, velocity, acceleration, and flap angle data. This can either originate from a prescribed-motion input file, or the model can be combined with the simulation framework presented in Section 4 to yield an outer solution loop for vessel motions and flap angle commands resulting from kinematic properties and flight control system algorithms.

3. Validation

The developed code is intended for evaluation of the performance of full-scale hydrofoil vessels, where high Reynolds numbers lead to turbulent flow along the majority of the hydrofoil surfaces. The authors do not know of any high-quality controlled hydrofoil experiments at sufficiently high Reynolds numbers to allow for direct experimental validation. Among published hydrofoil experiments which include a free surface, the ones with the highest Reynolds numbers identified by the authors are those of Wadlin et al. (1955) and Wilson (1983). They were performed at $Re \approx 2.0 \times 10^6$ and $Re \approx 3.41 \times 10^6$, respectively. Data from Hoerner (1965) and Silverstein and Becker (1939) indicates that frictional drag can often not be predicted by assumptions of fully turbulent flow until Reynolds numbers of approximately 1×10^7 for foil of smooth surface finish, such as was the case for the Wadlin et al. (1955) experiment. Silverstein and Becker (1939) observed that the location of the boundary layer transition point moves significantly with changes in the angle of attack in the Reynolds number regime of 1.73×10^6 and 5.02×10^6. They also found that thinner foil profiles, such as those typically employed in hydrofoil experiments, experience transition at more downstream positions than thicker foil profiles. The end of the transition region for a 12% thick hydrofoil at $Re = 3{\times}10^6$ was found at approximately the 43% chord position. This indicates that it will make little sense to compare drag values between our NDLL, which assumes fully turbulent flow in the creation of 2D models, and these experiments.

To overcome the challenge of a lack of experiments for direct validation of the NDLL, we propose a stepwise validation approach, where we compare results to those from three different data sources:

1. High-Reynolds-number aerodynamic experiments.
2. Hydrodynamic experiments with free surface proximity and incoming waves.
3. RANS generated datasets for steady and unsteady lift, drag, pressure distribution, and wake flow.

Table 1
Jacobs and Clay (1936) experimental data.

Parameter	Value
Span [inch]	30
Chord [inch]	5
Re	3.09×10^6
Re_e	8.16×10^6
Planform	Rectangular
Profile	NACA 23012
Twist	None

The philosophy behind the three-step validation process is the following. The field of aerodynamics has produced high-quality high-Reynolds-number experimental data. This can be used for validation of steady-state lift and drag predictions, but does not include the effects of free surface proximity or incoming waves. The mentioned hydrodynamic experiments, although not accurate for drag forces, can provide a validation of the effects on lift forces from incoming waves and free surface proximity. The final and most comprehensive step of the validation process is to compare NDLL results with those from 3D RANS simulations. These assume fully turbulent flow and hence equal profile properties to those modelled in the NDLL, allowing comparison of both lift and drag. Here we have the benefit that we can choose geometries and operating conditions which are more representative of hydrofoil vessels than those used in the aero- and hydrodynamic experiments. We can also compare all relevant aspects of the NDLL predictions, including steady and unsteady lift, drag, pressure distribution, and wake flow. The latter dictates interaction effects and the need for twisting downstream hydrofoils.

All RANS simulations are set up by a scripted approach, ensuring consistent meshing and solution settings. Details on the setup can be found in Appendix A. Here, we also present a refinement study for quantifying the numerical uncertainty of the simulations. To ensure trustworthy results, we include RANS simulations in the experimental validation steps.

A refinement study has been performed for the results of NDLL simulations, ensuring negligible effects of further refinement in space and time. The details of this can be found in Appendix C.

3.1. Aerodynamic experiment

In the early days of aviation, NACA produced a vast amount of experimental data on the aerodynamics of wing shapes, with effective Reynolds numbers in the range of 2×10^6 to 8.16×10^6. Many of these originate from large wind tunnel facilities such as the Variable-Density Wind tunnel (Stack, 1931; Eastman et al., 1935; Jacobs and Clay, 1936; Anderson, 1938) and the NACA Full-Scale Wind Tunnel (Silverstein, 1934; Silverstein and Becker, 1939; Goett and Bullivant, 1938; Bullivant, 1941). We find the experiments of Jacobs et al. (1935), Jacobs and Clay (1936) particularly interesting. After a correction for wind tunnel turbulence (Platt, 1936), these were performed at a particularly high effective Reynolds number of $Re_e = 8.16 \times 10^6$. The effective Reynolds number is here defined as the Reynolds number at which a non-turbulent flow would yield the same drag coefficient on a sphere, as that in the flow in the wind tunnel (Jacobs and Clay, 1936). Key data for the experiment are listed in Table 1.

Fig. 8 shows the correspondence between NDLL and experimental data. The NDLL results are produced at a Reynolds number corresponding to the *effective Reynolds number* in the Jacobs and Clay (1936) experiments. Simulations with XFOIL and RANS-based 2D models are included, with subscripts X2D and R2D, respectively. It is evident that the NDLL is able to reproduce the experimental data with great accuracy. NDLL results using the RANS-based 2D model yield better correspondence with the experimental data and 3D RANS data than those using an XFOIL-based 2D model. 3D RANS results, shown with subscript RANS in Fig. 8, also correspond well with the experimental

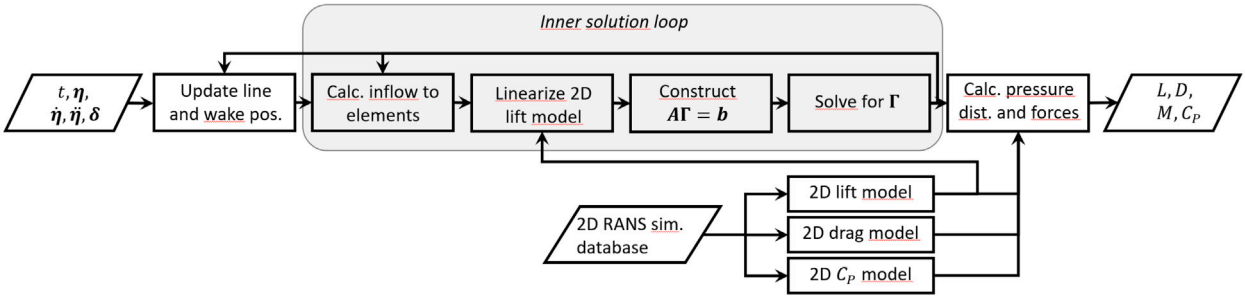

Fig. 7. Flowchart of the workings of the NDLL model.

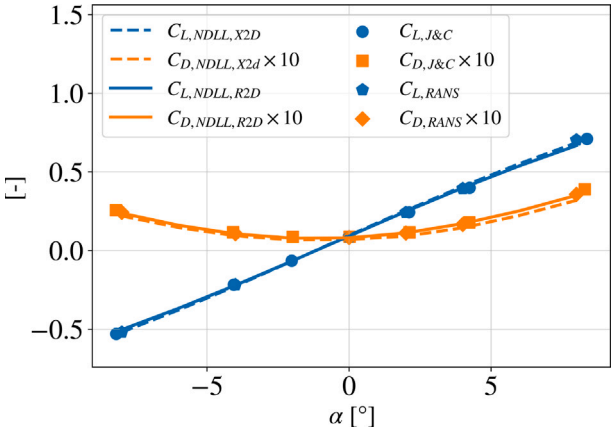

Fig. 8. Lift and drag coefficients compared with those of the aerodynamic experiment of Jacobs and Clay (1936). NDLL results with XFOIL and RANS 2D models, as well as 3D RANS results, are included.

data of Jacobs and Clay (1936). The fact that C_D results are accurately predicted by RANS with no turbulence transition model, combined with the fact that the RANS-based 2D model yields the best correspondence between NDLL and experimental data, indicates that most of the boundary-layer flow was fully turbulent in the experiment.

The range of $-4° \leq \alpha \leq 4°$ represents a wide estimate of the operating envelope of a hydrofoil vessel, which would have its range of angles of attack limited by cavitation constraints. The largest deviations between NDLL and 3D RANS simulations is here $\Delta_R C_D = 0.00052$ and $\Delta_R C_L = 0.0058$. Δ_R denotes deviation from 3D RANS data. The largest percentage difference in C_D is 3.1%. The percentage difference in C_L naturally spikes close to $C_L = 0$. A more interesting metric is here to compare the deviations with the mean C_L of a hydrofoil vessel. Using the value for the NTNU HFF1, presented in Appendix E, this constitutes a relative deviation of 1.8%.

Appendix A presents an evaluation of the numerical uncertainty in the 3D RANS data. An equivalent evaluation of the numerical uncertainty of the 2D data used as input for the NDLL is presented in Appendix B. Appendix C combines these estimates with the numerical uncertainty of the NDLL to estimate the validation uncertainty when comparing results from the two. As pointed out, the method for estimating numerical uncertainties is sensitive to the choice of input cases, making it challenging to draw hard conclusions on the exact magnitude of the validation uncertainty. We do however argue that it is likely to be in the range of 4.0–5.1%. Appendix B also points out that some systematic differences in profile properties are expected between unsteady simulations with unstructured meshes, such as those used in the 3D RANS, relative to those of steady simulations on structured meshes. The latter is used in the 2D models used as input to the NDLL. The observed correspondence between NDLL and 3D RANS is hence likely within the expected range posed by validation uncertainty and systematic differences in the evaluation of profile properties.

The largest deviations between NDLL and experimental data are $\Delta_E(C_D) = -0.00091$ and $\Delta_E(C_L) = 0.0166$, with $\Delta_E(x)$ denoting the deviation from experimental data of parameter x. No quantitative estimate of experimental uncertainty is given by Jacobs and Clay (1936), although a reference is given to Jacobs and Abbott (1933) for some estimates of certain effects. A series of known and typical experimental uncertainties are mentioned, including support interference, flow speed variations, and inaccuracies in the angle of attack. On top of this comes uncertainty in the estimation of the effective Reynolds number and any geometrical inaccuracies. As an example, $\Delta_E(C_L)$ corresponds to a potential deformation or misalignment of the wing relative to the inflow of 0.15°. The largest value of $\Delta_E(C_D)$ happens at $\alpha = -4°$, when $C_L/C_D \approx -18.5$. If the force transducer was misaligned with the inflow direction by as little as 0.25°, then this would explain the whole deviation. 3D RANS deviates from the experimental data by −0.00076 at the same data point, indicating that observed deviations might to a large extent originate from experimental uncertainty. We conclude that all observed deviations between NDLL and experimental data are likely within the combined experimental and numerical uncertainty.

3.2. Hydrodynamic experiments

Having established that the NDLL provides good lift and drag predictions at high Reynolds numbers in infinite fluid, the next step is to investigate its abilities to predict hydrodynamics-specific phenomena. In this section, we use experimental data from towing tanks to investigate the accuracy of lift variations due to free-surface proximity and incoming waves.

3.2.1. Wadlin, 1955

Wadlin et al. (1955) performed a series of hydrodynamic experiments on hydrofoils at various submergences. Key details of the experimental data used for validation herein are presented in Table 2. We evaluate the ability of the NDLL and RANS simulations to capture shallow-draft free surface effects by comparing the relative change of lift between deep and shallow operating conditions. This minimizes the impact of low-Reynolds-number effects on the comparison. There is some scatter in the results of Wadlin et al. (1955), the effect of which is minimized through the use of data from interpolation curves included in their plots.

Fig. 9 shows the ratio of C_L to that at "infinite" submergence, for submergence-to-chord values of 0.59 to 4.09. The experimental results show a significant reduction in C_L at submergence-to-chord of 4.09 relative to that at 3.09. This is believed to have been caused by some error, leading us to exclude the point from the comparison. Our "infinite" submergence case is hence that of h/c = 3.09.

It is evident that the NDLL is able to accurately predict the effect of the presence of a free surface for h/c values of 1 and higher, with all relative lift values corresponding to within 2% of those in the experimental data. For h/c = 0.59 the ratio of C_L to that at infinite depth is 7.5% higher for the NDLL than in the experimental data. It is deemed likely that a hydrofoil vessel of fully submerged hydrofoil

Table 2
Key data of Wadlin et al. (1955) and Wilson (1983) experiments used for validation herein.

Parameter	Wadlin et al.	Wilson
Span [inch]	32	96
Chord [inch]	8	16
Re	2.0×10^6	2.95×10^6
Fn_c	7.6	3.04
Submergence [c]	0.59–3.09	1.0
Surface finish	Smooth	Not given
Turbulence stim.	None	0.016 in. wire
Planform	Rectangular	Rectangular
Profile	$NACA64_1$ A412	NACA 64 A010
Twist	None	None
α	0°	4°

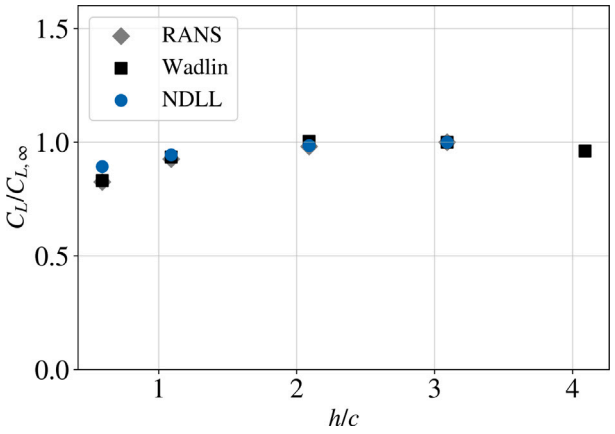

Fig. 9. Ratio of C_L to C_L at "infinite" submergence, the latter defined as h/c = 3.09.

design will be designed with h/c ≥ 1.0, as this reduces detrimental effects on lift and lift–drag ratio from the free surface, relative to operation at shallower drafts. Hence, a slight overprediction of lift at shallower drafts will likely not impact the typical vessel analysis. It is important to note that this does not hold true for hydrofoil systems with surface-piercing lifting surfaces. Parts of such hydrofoils will operate at h/c-ratios all the way to zero. The accuracy of the presented NDLL code has not been investigated for such cases. Additionally, it lacks corrections for spray drag and ventilation, which could be relevant in surface-piercing hydrofoil systems. The code should hence not be used for analysing surface-piercing hydrofoil systems until further extensions have been implemented, and an extended validation study has been conducted, evaluating the accuracy of the method for analyses of this type of hydrofoil systems.

The RANS simulation results correspond very well to the experimental data throughout the range of tested h/c values, indicating that it accurately captures free-surface effects.

3.2.2. Wilson, 1983

The final step of our experimental validation is an investigation of the accuracy of wave-induced forces at high encounter frequencies. Wilson (1983) performed towing-tank tests of a rectangular hydrofoil of NACA 64 A010 section in calm water and regular waves. Moderate Reynolds numbers of 0.98×10^6–3.41×10^6 were obtained, and encounter frequencies ranged from $k_e = 0.1$ to $k_e = 0.5$. We choose to re-create his experimental results for h/c = 1.0, at $Fn_c = 3.66$.

Due to low Reynolds numbers, the results of Wilson appear to have significant small-scale effects. Fig. 10 shows the linear lift slope of Wilson (1983), together with results from 3D RANS simulations and NDLL, at $h/c = 1.0$. The latter uses a 2D lift model from RANS. The analytical solution for an aspect ratio 6 hydrofoil at high submergence Froude number in inviscid flow is shown for reference. Corrections

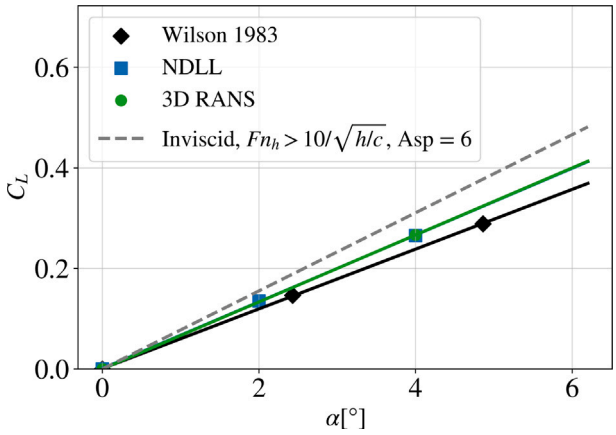

Fig. 10. Calm-water lift slope of Wilson (1983), 3D RANS and NDLL. The latter uses RANS-based 2D lift models. Lines are linear curve fits. The analytical solution for a hydrofoil of aspect ratio 6 operating at $Fn_h > 10/\sqrt{h/c}$ (Faltinsen, 2005) in inviscid flow is shown for reference.

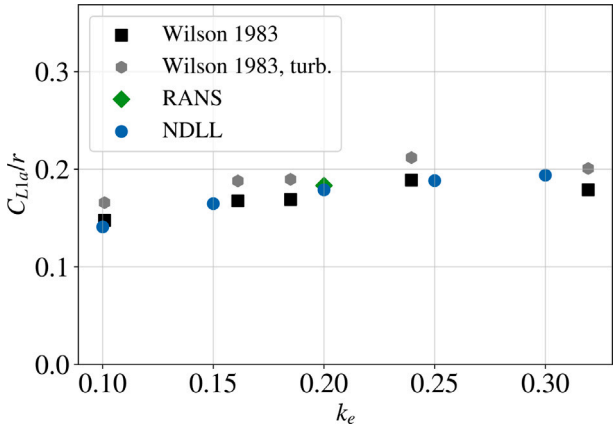

Fig. 11. The ratio of the C_L amplitude to the dimensionless parameter $r = \zeta_a/(0.5c)$, where ζ_a denotes the wave amplitude. Experimental results of Wilson (1983), NDLL results, and a 3D RANS result.

for aspect ratio and free surface have been made to the analytical solution, according to procedures presented by Faltinsen (2005). The free surface model assumes a submergence Froude number, Fn_h, higher than $10/\sqrt{h/c}$. It is evident that the slope of the Wilson results is lower than that predicted in turbulent flow conditions by 3D RANS and NDLL. Since we have already established the ability of the latter to describe 3D lift at high Reynolds numbers and to accurately capture near-surface effects, there is reason to believe the difference originates from scale effects in the experiment. The fact that 3D RANS and NDLL correspond to within 0.5% also strengthens this hypothesis. The lower lift slope might be related to laminar separation or separation on turbulence stimulator piano wires. The slope of the 3D RANS results is 12.2% higher than that of the experimental data.

Fig. 11 shows the ratio of the lift coefficient amplitude C_{L1a} to the dimensionless wave amplitude $r = \zeta/(0.5c)$, for the experiment of Wilson (1983), NDLL simulations, and a RANS simulation. ζ denotes wave amplitude. We have included a modified version of the results of Wilson with all C_{L1a} values multiplied by a factor of 1.122, i.e. scaling them by the ratio of steady-state lift slopes in Fig. 10. These are marked *turb.* and represent an estimate of experimental results with fully developed turbulent flow. This constitutes a coarse estimate, since the correction factor originates from steady-state cases. The magnitude of differences between scaled and unscaled results does however yield an impression of the magnitude of impact of laminar-flow effects of C_{L1a}/r.

All NDLL results correspond well with the experimental data, within the apparent scatter and expected deviations due to laminar-flow effects. In addition to differences related to the assumption of fully turbulent flow at relatively low Reynolds numbers, some deviations might be connected with dynamic separation effects. This is because the NDLL uses 2D lift models from steady-state 2D RANS simulations. Considering the scatter of experimental results, as well as the uncertainty which is inherently present in a low-Reynolds-number experiment, the correspondence between experimental data and NDLL results is judged as very good.

Due to limitations on computational resources, only one encounter frequency is replicated in RANS. Fig. 11 shows that the correspondence with experimental results, as well as NDLL results, is good. The difference between RANS and NDLL lift amplitudes is only 2.4%. Referring to Appendix C, this is likely within the validation uncertainty when comparing with 3D RANS.

All NDLL simulations were performed to an end time of 2.5 encounter periods. $C_{L1a/r}$ was compared between the last two periods, yielding less than 0.1% difference in all cases except $k_e = 0.3$, where the difference was 0.4%. To increase the computational efficiency in these relatively long simulations, NDLL results were obtained with a relatively short wake length of 10 chord lengths. Re-doing the case of $k_e = 0.20$ with a wake length of 15 chord lengths shows an increase in $C_{L1a/r}$ of 0.7%. This reduces the difference between NDLL and 3D RANS lift amplitudes to 1.7%.

3.3. RANS simulations of a realistic hydrofoil

The final validation step consists of comparing NDLL results of simulations of a representative hydrofoil geometry in realistic operating conditions, with those from 3D RANS simulations. Efforts have been made to generate a geometry which mimics the features of modern concept vessels for zero-emission hydrofoil passenger fast ferries presented by industrial companies. Details on the design philosophy, as well as the geometry itself, can be found in Appendix E. The geometry is hereafter termed the NTNU HFF1 (NTNU Hydrofoiling Fast Ferry 1), and can be found on the FASTSHIPS website (Godø and Steen, 2023) for easy use in future works.

We simulate the hydrofoil system of the vessel operating under a free surface in calm water and regular head waves. For the latter, we choose a case with high encounter frequency and relatively steep waves. This ensures the case is challenging with respect to dynamic lift effects, as well as ensuring the triggering of leading-edge cavitation. Carter (1982) presents formulae for the significant wave height and spectral maximum period as a function of the fetch distance and wind strength. A 12 km fetch distance, representative of a short fjord crossing, combined with 15 m/s wind, yields $H_s = 0.85$ m, $T_0 = 3.52$ m. Using the average chord length and design speed of the NTNU HFF1 main hydrofoil, this yields a reduced frequency of encounter $k_e = 0.173$. The latter is defined as $k_e = \frac{\omega_e c}{2U}$. An irregular sea state will contain waves of higher frequency and height than these spectral key figures. In the spirit of creating a challenging test case, we use $k_e = 0.20$, $H = 1.0$ in our regular-waves test case.

All simulations of the NTNU HFF1 use 2D models for C_L, C_D, and C_p based on steady 2D RANS simulations using structured meshes. As discussed in Appendix B, we have observed systematic deviations in profile data between results obtained with such, as compared to 2D simulations obtained with unsteady simulations with unstructured meshes. Since we are interested in evaluating the ability of the NDLL to accurately model hydrofoils, it is judged reasonable to minimize additional discrepancies between NDLL and 3D RANS originating from differences in profile modelling. All simulations of the NTNU HFF1 have therefore been performed with 2D models in which we have scaled C_L and C_D by 1/1.005 and 1/1.032, respectively. This yields profile data which converge approximately towards the same values as would be the case if they were obtained with unstructured meshes and unsteady simulations.

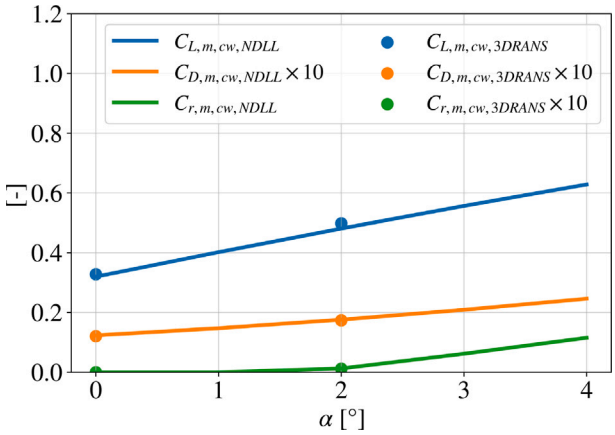

Fig. 12. Mean lift and drag coefficients, as well as average cavitating area coefficient, defined in Eq. (9), as a function of angle of attack. All results are for the main hydrofoil of the NTNU HFF1, detailed in Appendix E. NDLL results are compared to those from 3D RANS for calm water conditions at the design draft.

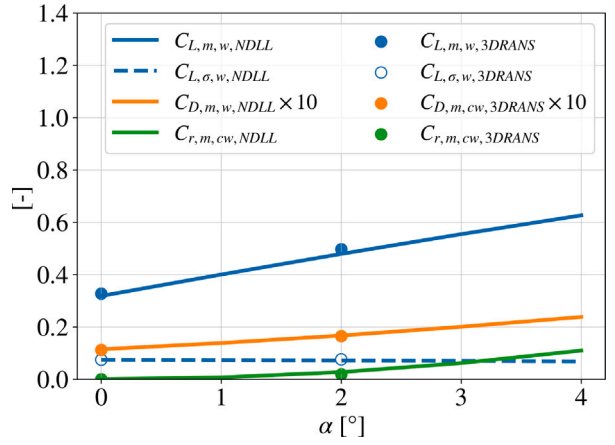

Fig. 13. Mean lift and drag coefficients, the standard deviation of the lift coefficient, and the average cavitating area coefficient, defined in Eq. (9), as a function of angle of attack. All results are for the main hydrofoil of the NTNU HFF1, detailed in Appendix E. NDLL results are compared to those from 3D RANS for regular waves of amplitude 0.5 m, $k_e = 0.20$ at design draft.

All simulations in this section are performed at 70% scale, yielding Reynolds numbers in the same range as used in validation against experimental data. The hydrofoil moves forward with a constant speed, and is restrained from any motion in response to hydrodynamic forces.

Fig. 12 shows C_L, C_D, and C_r as a function of angle of attack α, as predicted by the NDLL and by 3D RANS simulations. C_r denotes the average relative cavitating area through an encounter period, as defined in Eq. (9). The results from NDLL and 3D RANS correspond very well. Both C_L and C_D correspond within 3.5% for all data points, which is likely within the validation uncertainty as detailed in Appendix C. Predictions of C_r correspond within 6.9%. The absolute difference is however only 0.08 percentage points of the wetted surface, which is obviously well within the uncertainty present in the 3D RANS data.

Fig. 13 shows the same data as Fig. 12, for the case of regular head waves of $H_s = 1.0$ m, $k_e = 0.20$. It also includes the parameter $C_{L,\sigma}$, denoting the standard deviation of lift through one encounter period. This constitutes a metric for dynamic lift forces. Again, we can see that the correspondence between 3D RANS and NDLL is very good. At $\alpha = 0$ both $C_{L,m}$, $C_{L,\sigma}$, and $C_{D,m}$ correspond within 2.7%. C_r takes very low values in all compared cases, making relative errors large. The largest

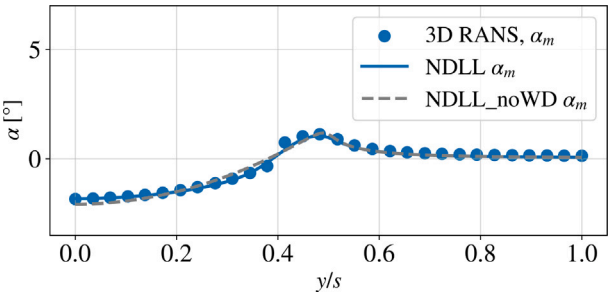

Fig. 14. Wake flow angles at z = −2.0 m, 10 m downstream of the main hydrofoil of NTNU HFF1. Predictions by RANS and two versions of the NDLL.

deviation between predictions by NDLL and 3D RANS is, however, less than 0.9 percentage points of the wetted surface.

Fig. 14 shows the wake flow angle α_w along a wide range of spanwise positions, 10 m = 11.20 mean chord lengths downstream of the main hydrofoil of the NTNU HFF1, at a depth of 2.0 m. This corresponds approximately to the streamwise and vertical coordinates of the quarter-chord of the tail hydrofoil. We have included results from two NDLL simulations, with and without wake deformation. The former utilizes the efficient wake deformation algorithm described in Section 2. It is seen that the correspondence between results with wake deformation and those from RANS is very good. Except for the immediate proximity of the tip vortex, all NDLL results are within 0.1° from those predicted by 3D RANS. The peak error is 0.33° at the location of the tip vortex. Due to the long convection distance and the well-known numerical dissipation found in RANS simulations, it is not clear whether it is the RANS or NDLL results which are closest to a physically correct value.

Results without wake deformation yield slightly larger errors from midspan to $y/s \approx 0.55$. Wake deformation acts, in this case, to flatten the curve of inflow angles for y/s values lower than the tip vortex position. The peak of induced inflow angles is also positioned at a lower value of y/s when accounting for wake deformation, indicating a slight contraction of the wake. In the non-deforming wake case, the tip vortex will naturally be positioned at $y/s = 0.5$. The differences between the deforming-wake and non-deforming-wake cases would likely be larger if not using a smooth circulation distribution as the currently applied bell shape.

The pressure distribution of the main hydrofoil of NTNU HFF1 in calm water at $U = 35$ knots, $\alpha = 2°$, is shown in Fig. 15. The two halves of the plot are predictions by the NDLL and 3D RANS simulations, respectively. The correspondence between the two is good, indicating that the NDLL accurately predicts the pressure distribution on hydrofoils. It can hence be used for predicting the inception of cavitation, keeping in mind that no direct modelling of the physics of cavitation itself is included. This means the results should not be relied on in cases where a significant portion of the wetted surface is found to have local pressures below the vapour pressure. The validation uncertainty for the local pressures when compared to 3D RANS is expected to be equal to or higher than that for C_L, since the latter is an integral quantity of the former. The slight discrepancy in trailing edge position between the halves is caused by a technical issue with the export of pressures from 3D RANS, leading to the exclusion of the downstream 1% of the chord length in exported pressure values.

4. Simulator

To allow simulations of free-running hydrofoil vessels under active control, we have created a simulator framework in which the NDLL is integrated. This consists of force, control system, and kinetics and kinematics modules. It allows simulations of a closed-loop system, in which the control system module dictates geometry changes in the force module, e.g. in the form of flap deflections in the NDLL model. The programme structure is shown in Fig. 16. ϕ_c, θ_c, ψ_c, and z_c denote commanded roll, pitch and heading angles, and flight height, respectively. The modules can be updated at different rates, enabling the simulation of fast-response physics like control system dynamics at a higher frequency than slower-response phenomena such as vessel kinetics and kinematics.

4.1. Control system module

The control system module takes commanded states and vessel motion data as input and outputs desired geometry changes in the form of flap angles or foil rotations to the force module. It is flexible with respect to control algorithms and currently contains a default hydrofoil control system based on separate PID loops with acceleration feedback in roll, pitch, heave, and yaw rate. Automatic tuning methods have been implemented. These approximate controller gains to achieve prescribed values of relative damping ratio and controller bandwidth, based on hydrofoil dimensions and placement, control surface dimensions and placement, and inertial properties. The method of pole placement of PID controllers with acceleration feedback of Fossen (2011) is used. More details can be found in Section 5.1.1. No observer or servo models are currently included, implicitly assuming perfect state observation and control surface actuation.

4.2. Force module

The force module sends commanded geometry changes and current environmental conditions as input to a set of force models. These then calculate forces and the force module sum and pass the resulting 6-DOF vessel-oriented force vector to the kinetics and kinematics module.

Force models currently comprise the NDLL model, a gravity model, an inertial model, and a constant-thrust propulsion model.

4.3. Kinetics and kinematics module

The kinetics and kinematics module calculates vessel motions based on forces and inertial properties. The kinematics module handles the relation between a global reference North-East-Down (NED) reference frame and a vessel-fixed BODY reference frame. It follows the kinematics conventions presented by Fossen (2011).

The kinetics module sums forces, calculates instantaneous acceleration and steps the solution in time to yield new velocity and position values. We use the vectorial notation of marine craft dynamics, first introduced by Fossen (1991). With modifications for the current case, we get Eq. (18). $\boldsymbol{M}_{RB}$ is the rigid-body system inertia matrix, containing the linear and rotational mass properties of the vessel. $\boldsymbol{C}_{RB}$ denotes the Coriolis-centripetal matrix and $\boldsymbol{\tau}_{FM}$ is the sum of forces as transformed into the BODY frame. This includes gravity, propulsion, and hydrofoil forces. $\boldsymbol{\nu}$ is the 6-DOF body-frame velocity vector containing linear and angular velocities.

$$\boldsymbol{M}_{RB}\dot{\boldsymbol{\nu}} + \boldsymbol{C}_{RB}(\boldsymbol{\nu})\boldsymbol{\nu} = \boldsymbol{\tau}_{FM} \tag{18}$$

The transformation from BODY to NED velocities is done by Eq. (19), where $\boldsymbol{J}_{\Theta}$ is a 6-DOF matrix containing linear-velocity and angular-velocity transformation matrices.$\boldsymbol{\eta}$ denotes the 6-DOF position and attitude vector in the NED frame. See Fossen (2011) for details. A choice between Euler and Adams–Bashforth time integration is allowed when stepping the solution of η in time.

$$\dot{\boldsymbol{\eta}} = \boldsymbol{J}_{\Theta}(\boldsymbol{\eta})\boldsymbol{\nu} \tag{19}$$

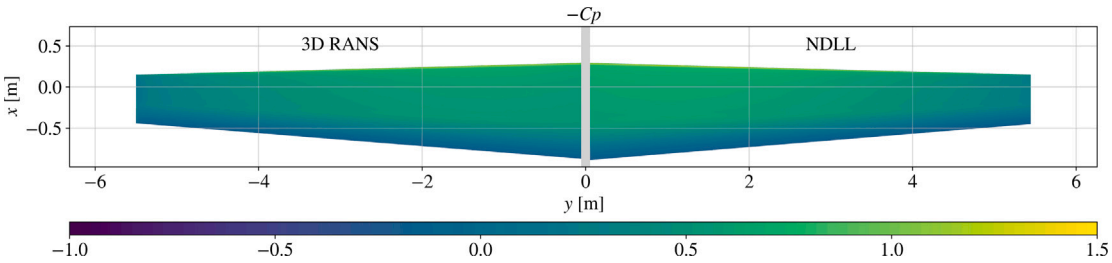

Fig. 15. Pressure distribution on the main hydrofoil of NTNU HFF1 in steady-state conditions, as found by NDLL and RANS. U = 35 knots, $\alpha = 2°$. Flow direction from top to bottom.

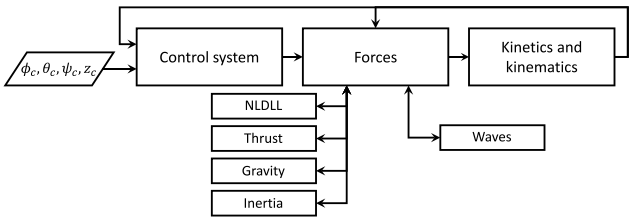

Fig. 16. Simulator overview. ϕ_c, θ_c, ψ_c, and z_c are commanded roll, pitch and heading angles, and flight height, respectively.

4.4. Implementation

The software is an object-oriented Python code with a modular structure to allow easy extension. It is part of the FASTSHIPS (Fast And Simple Tool for Simulation of HIgh Performance Ships) software package of the NTNU Department of Marine Technology (Godø and Steen, 2023).

The modular design allows the addition of new force modules such as aerodynamics or hull hydrodynamics, the implementation of new control algorithms or the addition of new modules for state observation or actuator system simulation. Current work constitutes the first step on the way to providing a full hydrofoil dynamic simulation capability incorporating all relevant physics for virtual testing of new vessel or vessel systems designs.

5. Case study

This section presents a use case for the presented hydrofoil simulation method. It involves a case study on vessel motions and added resistance in waves, specifically focusing on a fully foil-supported hydrofoil vessel operating in regular head waves. The simulation assumes that the hull is lifted sufficiently high to ensure no contact with the water and neglects aerodynamic forces on the hull and superstructure. These assumptions enable the simulation of hydrodynamic forces and motions of the vessel using the methods presented in the current paper.

The purpose of the case study is to verify the combined simulator and NDLL models, as well as their software implementations, and assess whether they produce reasonable results for simulating free-running hydrofoil vessels.

5.1. Case description

All test cases simulate the NTNU HFF1 vessel operating on straight-line trajectories at its design speed. The NTNU HFF1 was specifically designed for the studies presented in this paper. Detailed information on its geometry and inertial properties can be found in Appendix E. The vessel is free to move in four degrees of freedom, with sway and yaw forced to zero. The latter is done because of the absence of struts in the simulation, resulting in minimal damping in those degrees of freedom. Similar to Appendix C, a scale of 70% is used, resulting in Reynolds numbers approximately equal to those of the wind tunnel data used for validation in Section 3.1.

Nine simulations are performed, including one simulating the vessel in calm water and the remaining ones simulating operation in regular head waves. Eight encounter frequencies are studied, ranging from 0.2 Hz to 18.6 Hz. The wave height is set to 1.0 m.

The case study serves as a comprehensive test to verify that the kinematics and control system modules do not have any major bugs. It also confirms that the implemented control algorithms are capable of effectively controlling a hydrofoil vessel, that reasonable controller gains are found by our tuning methods, and that physically sensible flap commands are communicated between the controller and force modules.

It is important to note that the scope of this study is to verify the simulator code rather than fully map the dynamic behaviour of the studied vessel in waves. Nevertheless, valuable insights can be extracted from the simulation results regarding vessel response and added resistance of hydrofoil vessels in regular head waves. The variation in encounter frequencies allows for a rough mapping of the response amplitude operator (RAO) curves of the vessel under consideration. Future work should include studies on the linearity of vessel response and added resistance with wave height, as well as vessel behaviour in different wave directions.

5.1.1. Controller design

The flight control system is designed as a set of three independent PID controllers for heave, roll, and pitch. Each control loop is tuned using the pole placement method presented in Fossen (2011). All are tuned to a relative damping ratio of 1 without acceleration feedback. The bandwidths of the control loops are set to 5.0 s, 3 s, and 1.0 s for heave, roll, and pitch, respectively. This ensures sufficient bandwidth separation between heave and pitch dynamics to justify independent controllers. In the tuning process for the heave controller, a zero pitch angle is assumed.

Inertial moment arms for roll and pitch are assumed to be 1/3 of the vessel width and length, respectively. Natural system damping is estimated by considering lift from motion-induced angles of attack, as described by Eq. (20) (Faltinsen, 2005). Here, Λ represents the aspect ratio defined in Eq. (21), and s and S_{proj} denote span and projected area, respectively. In cases where the controller tuning method suggests the application of negative control system damping, the damping term is set to zero.

$$C_{L,\alpha} = \frac{2\pi}{1 + 2/\Lambda} \tag{20}$$

$$\Lambda = \frac{s^2}{S_{proj}} \tag{21}$$

When formulating the control configuration matrix, we make the assumption that control forces can be described by Eq. (22). In this equation, $\boldsymbol{\tau}$, $\boldsymbol{T}$, $\boldsymbol{K}$, and $\boldsymbol{u}$ denote control force, control configuration matrix, force coefficient matrix, and control input vector, respectively.

$$\boldsymbol{\tau} = \boldsymbol{T}\boldsymbol{K}\boldsymbol{u} \tag{22}$$

The force coefficient matrix, denoted as $\boldsymbol{K}$, is constructed based on the assumption that the 2D lift coefficients resulting from flap deflection follow the analytical expression presented in Eq. (23) (Faltinsen, 2005). In this equation, r and $C_{L,2D,f}$ denote the relative chord length of the flap and the 2D lift coefficient resulting from flap deflection, respectively.

$$C_{L,2D,f} = 8\sqrt{r}\alpha_f \tag{23}$$

The control configuration matrix, denoted as $\boldsymbol{T}$, is created by assuming that flap forces act at the quarter-chord position at the spanwise area centre of the flapped hydrofoil sections.

To solve the control allocation problem for $\boldsymbol{u}$, an unconstrained minimization of flap deflections is performed with equal weights assigned to all flaps. This reduces the problem to finding the Moore–Penrose pseudo-inverse of the control force configuration matrix (Fossen, 2011) and the inverse of the force coefficient matrix $\boldsymbol{K}$. The control input can then be determined using Eq. (24), where $\boldsymbol{T}^{\dagger}$ denotes the Moore–Penrose pseudo-inverse of $\boldsymbol{T}$.

$$\boldsymbol{u} = \boldsymbol{K}^{-1}\boldsymbol{T}^{\dagger}\boldsymbol{\tau} \tag{24}$$

5.2. Simulation method

The case study utilizes the NDLL-based hydrodynamic force model and the simulator framework described in Sections 2 and 4, respectively. The geometry and inertial properties of the hydrofoil vessel are presented in detail in Appendix E, and the control system algorithm and its tuning process are as described in Section 5.1.1.

Since the simulation assumes a fully lifted hydrofoil vessel with no parts of the hull touching the water, all hydrodynamic forces are acting on the hydrofoil system. The drag force can be extracted as the longitudinal component of the force output from the NDLL. Average values are obtained from calm-water and wave simulations by averaging over the last 10% of the simulation time and over the last encounter period, respectively. The relative added resistance in waves can then be calculated as the difference between the average resistance in a wave condition and that in calm water, expressed as a relative value.

By extracting the output from the kinematics and kinetics modules of the simulator, time series of the vessel's motion response are obtained. Similarly, time series of flap motions can be extracted from the output of the control system module. Amplitudes of vessel motion and flap angle responses are compared to the incoming wave amplitude to determine the *response amplitude operator* (RAO) mapping.

5.3. Results and discussion

The following sections present and discuss first the details of the calm-water simulation and one wave simulation, then the variations in added resistance and vessel response in various degrees of freedom as a function of encounter frequency.

5.3.1. Calm water

Fig. 17 illustrates the time series of flap deflection angles and vessel motions from the simulation conducted in calm water. The flaperons, denoted as SB flaperon and PS flaperon, are control surfaces that act as both ailerons and flaps, providing roll and heave forces on the vessel. They are positioned on the main hydrofoil, on the starboard and port sides, respectively. The elevator, a flap on the horizontal stabilizer, controls the vessel's pitch motion. Further details regarding the positions, shapes, and sizes of the flaps can be found in the vessel description provided in Appendix E.

The results indicate that the control system functions as intended in calm water, smoothly bringing all states towards their target values. In the converged condition, virtually no flap angle is applied, indicating that no steady-state correction is required to achieve force and moment balance in heave and pitch. This suggests that the design process outlined in Appendix E, including the positioning, wing twisting, and spanwise varying profile properties, successfully yields a geometry which generates the desired hydrodynamic forces and moments when operating at the design speed.

5.3.2. Regular waves, one encounter frequency

Flap angles and vessel motions for the case of $T_e = 0.56$ Hz are depicted in Fig. 18. Here, T_e denotes the encounter period of the waves. Again, the controllers successfully guide the states towards their target values, with small heave and pitch oscillations superimposed on the converging trends. The heave amplitudes measure 0.017 m, constituting only 4.9% of the incoming wave amplitude. It is evident that the controllers are working actively to counteract excitation forces from waves, by applying oscillatory flap angles. The elevator flap obtains the largest flap angle magnitudes of 3.5°.

An evaluation of the pressure distribution on the wetted surface during the last encounter period yields $C_r = 0.0001$ and $C_r = 0.0000$ for the main and tail hydrofoils, respectively. Here, C_r denotes the ratio of the average area below vapour pressure to the wetted surface area, as explained in Section 2.7. These results indicate that cavitation is practically absent on the hydrofoil system in question, despite the application of relatively large flap angles.

Fig. 19 presents a comparison of the longitudinal drag force on the NTNU HFF1 in calm water and waves, as extracted from the NDLL simulation. Average values are shown by dashed lines. The case with waves inherently incorporates the effects of increased profile drag and induced drag due to varying inflow angles and flap deflections commanded by the flight control system. It is worth noting that the drag in waves varies in a non-sinusoidal manner, with narrow low-valued regions and wide high-valued regions. Hence, the time-averaged value is not halfway between the high and low peaks.

An interesting observation arises from the data, revealing that the average resistance in waves is 1.7% lower than that in calm water. Initially, this may appear counter-intuitive. However, the phenomenon can be explained by the physics of wave propulsion hydrofoils (Bøckmann and Steen, 2013; Bøckmann, 2015; Bøckmann and Steen, 2016). When a hydrofoil travels through an oscillating flow field, as is the case when operating in waves, it experiences varying inflow angles and, consequently, varying angles of attack. When inflow comes from below, the angle of attack increases. This increases lift and tilts the lift vector slightly forward. This forward tilt arises because lift acts perpendicular to the inflow direction. Conversely, inflows from above decrease the angle of attack, leading to reduced lift and a slight backward tilt of the lift vector. Decomposing the time-varying lift vector in the horizontal plane reveals that the net effect of these variations is a forward thrust. The magnitude and direction of drag also oscillate with the variations in the inflow angle. Inflows from above reduce the local angles of attack, thereby decreasing drag, while inflows from below have the opposite effect. It has been observed that the net effect of these variations in the lift and drag vectors for a hydrofoil operating in a wave field can be a propulsive force (Bøckmann, 2015).

In the case of a wave propulsion foil mounted to a ship hull, the net change of resistance between calm water and waves will typically be positive. This is due to significantly increased hull drag caused by the reflection and radiation of waves (Faltinsen, 1990). However, in the context of a fully foil-supported hydrofoil vessel with no hull-water contact, it is not evident that the net added resistance in waves must be positive. Since there is no added resistance on the hull, if the hydrofoil system experiences a net reduction in resistance due to the relative motion between itself and the surrounding water, the net added resistance on the vessel can be negative.

For an actively controlled hydrofoil vessel, where the control system applies flap angles to regulate the vessel states, the hydrodynamic forces are modified compared to typical constant-geometry hydrofoils investigated in wave propulsion foil research. The effect of these changes might be either increased or decreased resistance, relative to

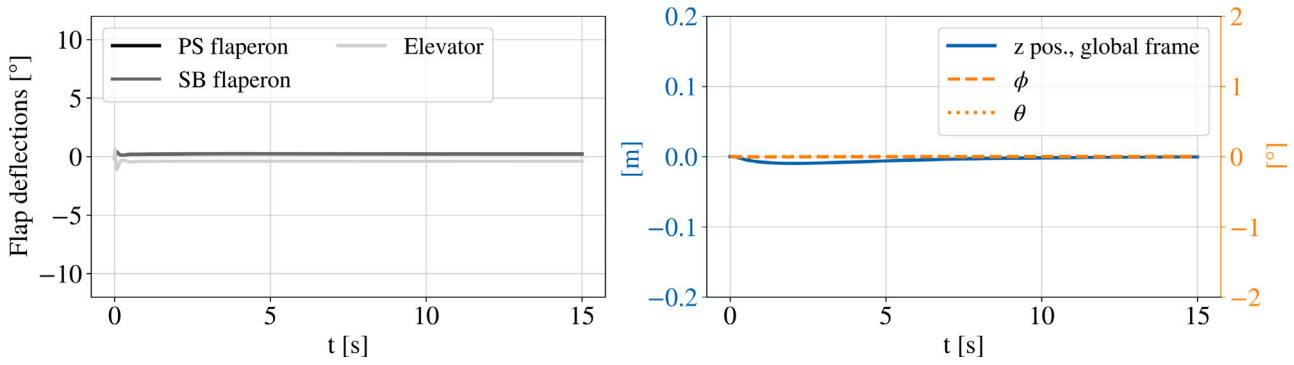

Fig. 17. Vessel motions and flap angles in 4-DOF calm water simulation of the NTNU HFF1.

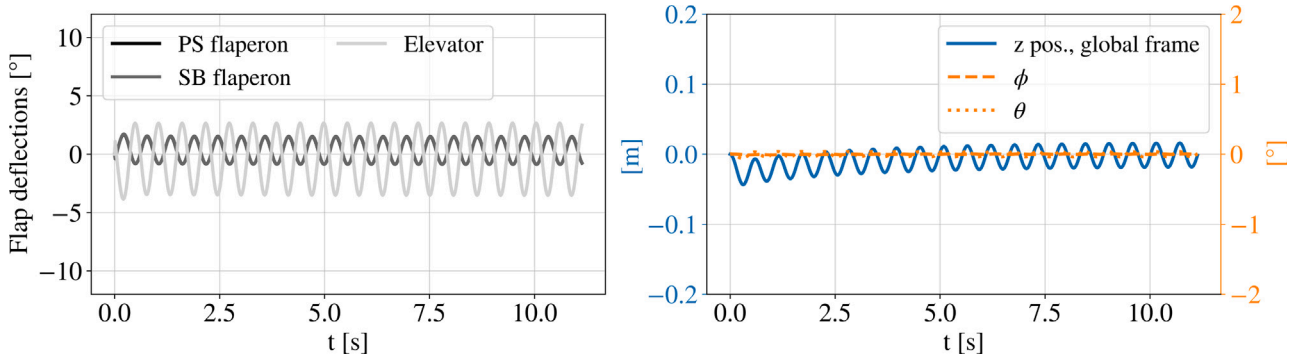

Fig. 18. Vessel motions and flap angles in a 4-DOF simulation of the NTNU HFF1 vessel in 1.0 m regular head waves at an encounter period of 0.56 s. Full-scale wave height $H = 1.0$ m.

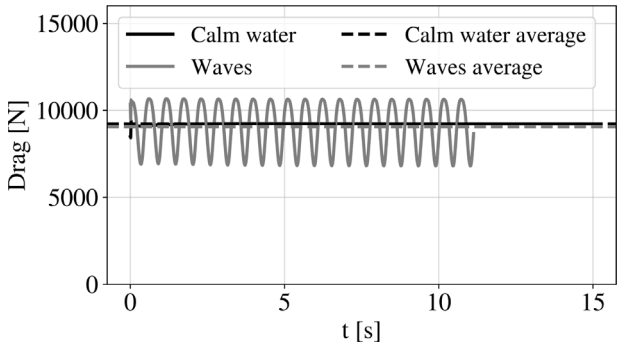

Fig. 19. Drag of the NTNU HFF1 in calm water and regular waves of an encounter period of 0.56 s. Full-scale wave height $H = 1.0$ m.

a constant-geometry hydrofoil. Even if an isolated effect of increased resistance occurs due to flap activation, it may not surpass the thrust provided by oscillations in the magnitude and direction of lift. Hence, the net added resistance of the vessel can still be negative.

These simulations inherently consider the effects of time-varying inflow angles and flap angles. However, it should be noted that the exclusion of struts in the current simulations could affect the presented results. We expect the effect of including struts in evaluations of added resistance in waves to be an oscillating change of resistance due to oscillating wetted surface area. The mean value of this is expected to be practically zero.

Added resistance in waves is likely to be a critical factor in the design of battery-powered fast ferries. A low or negative value of added resistance can provide a significant comparative advantage for hydrofoil vessels over conventional catamarans in terms of vessel weight and drivetrain cost.

5.3.3. Frequency-dependent variations

Fig. 20 illustrates the resistance, vessel response, and flap angle response of the NTNU HFF1 as a function of encounter frequency in head waves. In the figure, D_w and D_{cw} denote drag in waves and calm water, respectively. Consequently, resistance is presented relative to calm water conditions. ζ_a, z_a, θ_a, and f_x denote the wave amplitude, the heave response amplitude, the pitch response amplitude, and the response amplitude of flap x, respectively. The results reveal that the added resistance of the vessel can be either positive or negative, depending on the encounter frequency. The maximum magnitude of added resistance observed in the tested cases is only 2.7%, and it is negative.

A notable observation from Fig. 20 is the presence of a peak in the heave vessel response near an encounter frequency of 0.2 Hz. This corresponds to the bandwidth of the heave controller. Assuming a critically damped system, the closed-loop eigenfrequency in heave is 0.3 Hz. The peak in vessel response is likely attributed to excitation near the eigenfrequency.

Additionally, it is interesting to observe a local peak in the magnitude of added resistance at 1.4 Hz, albeit minor. Both the pitch response and the actuation of flap 3, which is the elevator flap on the tail hydrofoil, exhibit peaks near this frequency. The increased resistance is likely linked to increased profile and induced resistance on the tail hydrofoil due to large angles of attack and flap angles. The offset of the tail hydrofoil from the centre of gravity, combined with significant pitch amplitudes, contributes to large local angles of attack. We note that the bandwidth of the pitch controller is 1 Hz. Assuming again a critically damped system, the closed-loop eigenfrequency in pitch is 1.55 Hz. It is judged likely that the tuning of the pitch controller affects the placement of local resistance peaks in the frequency band.

The most significant changes in resistance are observed for the second and third-highest encounter frequencies, 2.57 Hz and 2.17 Hz, respectively. The corresponding wavelengths in these cases are 7.2 m and 8.6 m. These values closely align with the distance between the

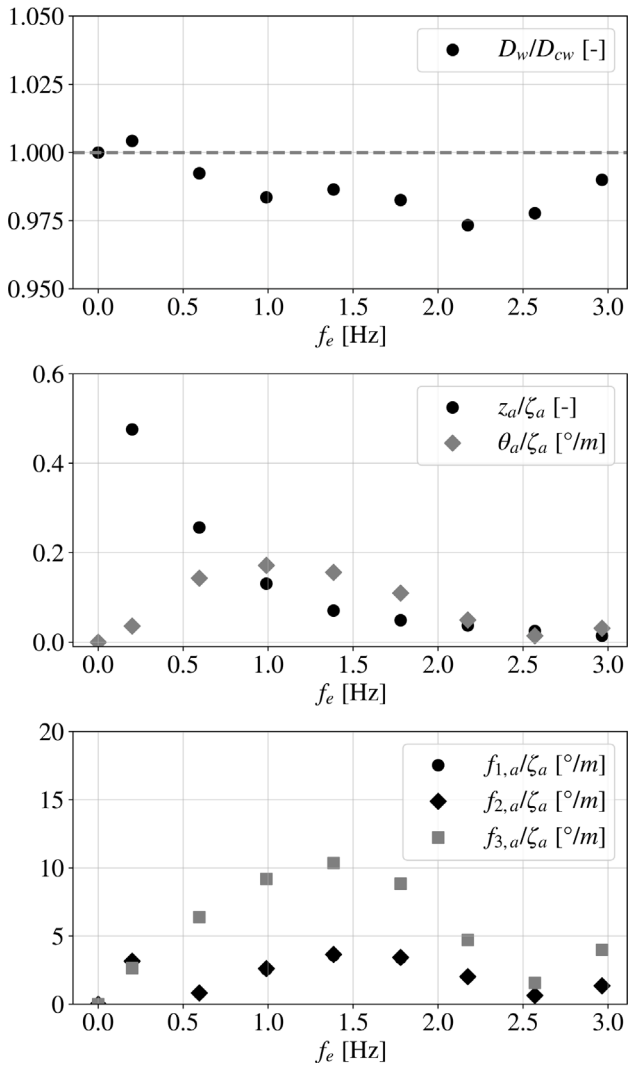

Fig. 20. Resistance, vessel motion response, and flap angle response as a function of encounter frequency. Flaps 1, 2, and 3 are the port side and starboard flaperons on the main hydrofoil, and the elevator on the tail hydrofoil, respectively.

main and tail hydrofoils, which is 7.8 m in the 70% scale simulation. As a result, the main and tail hydrofoils experience in-phase local vertical velocities from the undisturbed wave velocity field. A consequence of this is that the induced downwash on the tail hydrofoil from convected unsteady trailing vorticity from the main hydrofoil oscillates in phase with the wave-induced vertical velocities at the tail. Hence, when there is a peak in vertical wave-induced velocities on the tail, there is also a peak in downwash velocities from trailing vorticity originating from the upstream main hydrofoil. This partially mitigates the effect of wave-induced forces on the tail and, subsequently, the wave-induced pitch moments on the vessel. It is plausible that this phenomenon contributes to the local minimum in flap angles observed for the pitch and heave controllers at the second-highest encounter frequency, as well as the low value for the third-highest encounter frequency. This subsequently contributes to explaining the reduced resistance at these encounter frequencies.

It is important to note that the current study represents an initial investigation into the added resistance and vessel response of a specific hydrofoil vessel with a specific controller tuning. The number of encounter frequencies considered is limited, and only one wave direction has been studied. The primary objective of this section is to demonstrate the utility of the presented methods and gain preliminary insights into a physical problem. Since current results have not been validated against experimental data, further research is needed before concluding that negative added resistance in waves or other key findings of Section 5 are realistic.

The prospect of hydrofoil vessels experiencing negative added resistance in waves, to the best knowledge of the authors, has not been extensively studied or documented in the literature. Further research on this topic extends beyond the scope of the current work but is being pursued in a follow-up study. It is believed that a comprehensive examination of the effects of control system tuning and geometrical design on added resistance and vessel response can unlock new possibilities for designing energy-efficient hydrofoil vessels with excellent seakeeping abilities.

6. Conclusions

This work has presented a simulation tool for hydrofoil vessels based on Non-Linear Lifting Line (NDLL) methodology. Novel modelling approaches within this framework, verification, and validation studies, and a practical application of the methods have been presented and discussed.

In terms of simulation methodology, significant contributions have been made, including novel techniques for efficient modelling of wake deformation, the development of a hybrid wake model incorporating a quasi-steady downstream portion, an efficient approach for hydrofoil interaction calculations, and a new model for the viscous core of wake vorticity elements. Additionally, a novel approach based on matrix interpolation, along with spatial and temporal resolution reduction, has been introduced for the efficient calculation of Green Function contributions to the velocity potential.

The combination of these methods and submodels in a comprehensive tool for evaluating forces, pressure distribution, and vessel motion of actively controlled hydrofoil vessels is a unique contribution of this work, as far as the authors are aware.

A crucial aspect of this research is the thorough validation study, which involved comparing the NDLL model with experimental data from wind tunnel tests and towing tank campaigns, and a large set of new benchmarking results generated with 3D RANS simulations. Good accuracy was found for steady and dynamic forces, as well as wake flow angles and pressure distribution on hydrofoils, proving the worth of the presented model for the design and analyses of hydrofoil vessels.

The concluding case study not only verified the functionality of the code for its intended purpose, but also revealed an intriguing finding of the possibility of experiencing negative added resistance in waves for a hydrofoil vessel operating in head seas. The frequency dependence of this phenomenon was investigated, indicating that controller tuning and hydrofoil spacing play a crucial role in determining the encounter frequencies at which positive and negative resistance peaks occur.

Future extensions of the code will involve incorporating struts and accounting for the viscous interaction between struts and lifting hydrofoils. Additionally, a series of design studies and operational studies are planned to further enhance our understanding of how to create more efficient hydrofoiling fast ferries.

CRediT authorship contribution statement

John Martin Kleven Godø: Conceptualization, Methodology, Software, Formal analysis, Investigation, Writing – original draft, Visualization. **Sverre Steen:** Conceptualization, Supervision, Writing – review & editing, Project administration, Funding acquisition, Resources.

Declaration of competing interest

The authors declare that they have no known competing financial interests or personal relationships that could have appeared to influence the work reported in this paper.

Data availability

The geometry of the NTNU HFF1 vessel is published online and a reference is given in the article text.

Declaration of Generative AI and AI-assisted technologies in the writing process

During the preparation of this work, the authors used the AI-based spelling and grammar tools Grammarly and LanguageTool, as well as the language model ChatGPT by OpenAI, in order to improve the spelling, language, and grammar of this paper. After using these tools/services, the authors reviewed and edited the content as needed and take full responsibility for the content of the publication.

Acknowledgements

The presented work was financed by the ZEVS Project (The Research Council of Norway (RCN) Grant No.: 320659), SFI Smart Maritime (RCN Grant No.: 237917), and a development project for hydrofoil simulation tools in collaboration with Lift Ocean (RCN MAROFF-2 Grant No.: 295765). The majority of the RANS simulations, constituting approximately 1 million CPU hours, were performed on Uninett Sigma2 national high-performance computing resources as part of project NN9389K.

Appendix A. 3D RANS simulations

All RANS simulations presented in this study were conducted using OpenFOAM v2206, and the meshes were generated using the corresponding versions of the blockMesh and snappyHexMesh utilities. The simulations utilized a combination of computational resources from the NTNU Department of Marine Technology and national Norwegian High-Performance Computing, with a total CPU time of approximately 10^6 CPU hours. In the following sections, we provide detailed information on the simulation settings and present a refinement study that quantifies numerical uncertainty. The key settings used in the simulations are summarized in Table 3.

A.1. Simulation setup

A scripted approach was employed to ensure consistent settings across different cases in all simulations. Variations of the number of near-geometry prism layers and cell expansion ratios were necessary to achieve equal cell sizes adjacent to the prism layer for different Reynolds numbers. The subsequent sections detail the meshing, boundary conditions, waves, solver, schemes, and other relevant settings of the 3D RANS simulations.

A.1.1. Meshing

All meshes were generated according to the settings outlined in Table 3. In the table, h_x denotes the streamwise and vertical cell dimensions in region x, where regions A-D are defined in Fig. 21. The spanwise cell dimensions were twice the streamwise dimensions. c and s denote average chord length and span, respectively. For cases involving a free surface, a refinement zone was placed along the air–water interface. This had 34 and 78 cells per incoming wave height and 237 and 113 cells per incoming wave length, for the Wilson (1983) and NTNU HFF1 cases, respectively. The settings for the prism layers had to be adjusted for cases with different Reynolds numbers to ensure reasonable values of y^+, the number of layers, the expansion ratio, and the cell size transition to the cells adjacent to the prism layer In all prism layers, the inner cell height corresponded to $30 \leq y^+ \leq 55$, the outer cell height was 0.4 to 0.5 times the cell dimension in region A, and the layer expansion ratio ranged from 1.15 to 1.30.

Table 3
RANS settings.

Parameter	Value
y^+	30–55
h_{ref} $[c]$	$2^{\frac{2}{3}}$
h_A $[c]$	$1 \times h_{ref}$
h_B $[c]$	$4 \times h_{ref}$
h_C $[c]$	$8 \times h_{ref}$
h_D $[c]$	$64 \times h_{ref}$
Cells between ref. levels	4
Turbulence intensity at inlet	0.10%
Number of prism layers	2–5
Prism layer expansion ratio	1.15–1.30
Domain extent downstream	25 c
Domain extent upstream	10 c
Domain width, half	2.5 s
Domain h. abv. free surf.	max(5 c, 1 s)
Domain h. abv. geometry, inf.fluid	max(10 c, 2 s)
Domain depth below hydrofoil	max(10 c, 2 s)
Solution algorithm	PIMPLE
Number of outer solution loops	3
Number of inner solution loops	2
CFL_{h_A}	1
Turbulence model	SST k - ω
k wall function	*kLowReWallFunction*
ω wall function	*omegaWallFunction*

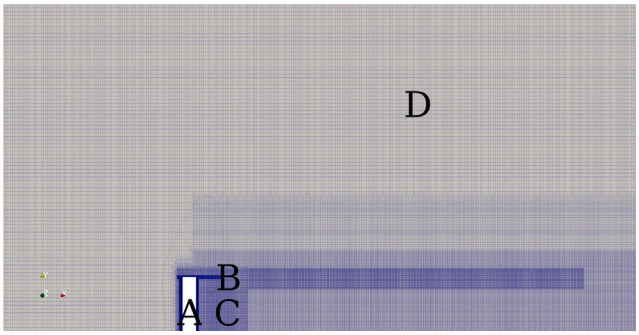

Fig. 21. Top view of mesh for 3D RANS simulation of the aerodynamic experiments of Jacobs and Clay (1936). Flow direction from left to right.

A.1.2. Boundary conditions

The simulation domain is meshed only for half of the geometry, assuming symmetry. Symmetry boundary conditions are applied to the symmetry, bottom, side, and top planes. At the outlet, zero velocity, k, and ω gradients are enforced, along with fixed pressure conditions.

A.1.3. Waves

In cases involving waves, linear Stokes waves are prescribed at the inlet, and a linear damping zone with quadratic damping is applied in the downstream region. The damping factor is set to 1.5 times the value recommended by Perić and Abdel-Maksoud (2016).

A.1.4. Solver, numerical schemes, and other settings

The PIMPLE solution algorithm, a combination of the PISO and SIMPLE algorithms, is employed in the solution process, with 3 outer loops and 2 inner/PISO loops. For cases with a free surface, the Volume Of Fluid (VOF) method is used to simulate the two-phase flow. The Euler scheme is used for time discretization. Convective terms are discretized using the linear upwind scheme, while k and ω are discretized with a Gauss limited linear scheme using a limiting coefficient of 1. All other quantities are discretized using Gauss linear schemes. The time steps correspond to a Courant number of 1.0, based on the near-geometry streamwise cell size.

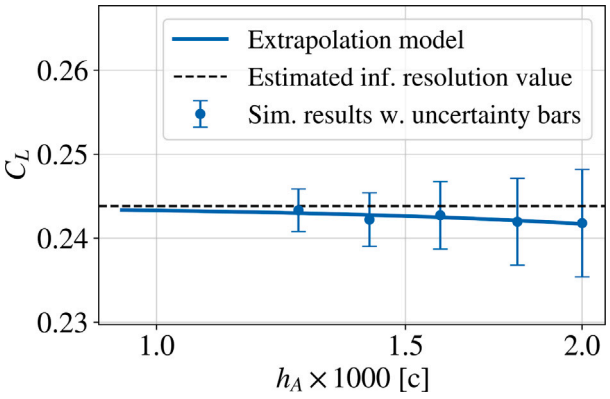

Fig. 22. Convergence and uncertainty estimates of C_L as a function of near-wing cell size h_A. The latter is measured in chord lengths. Error bars show the estimated uncertainty at the given refinement level.

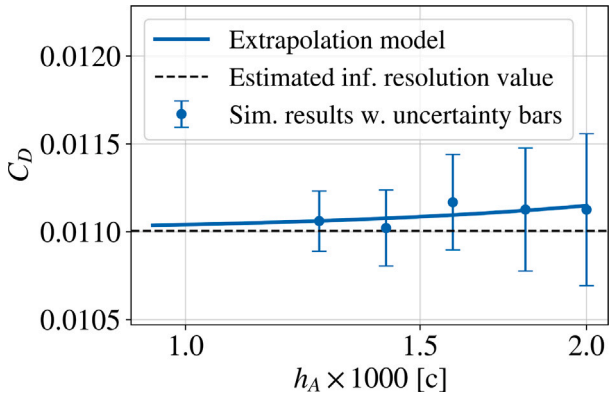

Fig. 23. Convergence and uncertainty estimates of C_D as a function of near-wing cell size h_A. The latter is measured in chord lengths. Error bars show the estimated uncertainty at the given refinement level.

A.2. Refinement study

The numerical uncertainty of 3D RANS simulations herein has been estimated using the method for error and uncertainty estimation by a least squares root approach outlined by the 28th ITTC Resistance Committee (2017). The wind tunnel case of Jacobs and Clay (1936), with the wing at $\alpha = 2°$, is used for this study.

Figs. 22 and 23 present convergence plots of the lift coefficient (C_L) and drag coefficient (C_D) for gradually refined meshes. The near-wing cell size (h_A) is measured in chord lengths. The error bars indicate the estimated uncertainty at each refinement level. The cell counts range from 17.9 million to 57.8 million. As observed from the figures, there is some scatter in the results, which likely originates from irregularities in the unstructured meshing process using the snappyHexMesh utility. Extensive testing of various settings has been conducted to minimize this scatter, and the presented simulations were performed with settings found to minimize it.

For all simulations in Sections 3.1 and 3.2 we use $h_{ref} = 2^{2/3} \times 10^{-3}$. This yields 32.5 million cells in the Jacobs and Clay (1936) case and is considered a reasonable compromise between numerical accuracy and computational resources. Following the ITTC procedure (28th ITTC Resistance Committee, 2017), the estimated numerical uncertainty for C_L and C_D is 0.0040 and 0.00027, respectively, corresponding to 1.7% and 2.4% of the absolute values. We emphasize that these are only estimates of the uncertainty. Removal of the finest test case reduces these estimates to 0.00109 and 0.00027, or 0.4% and 2.4% for C_L and C_D, respectively. Conversely, if the coarsest test case is removed, the equivalent estimates are 0.00482 and 0.00046 or 2.0% and 4.1%. It is judged likely that a slight shift of refinement levels in the test cases, alternatively the inclusion of more cases, would shift the estimates again.

Due to the high sensitivity to the choice of input cases in the method for estimating numerical uncertainty, it is hard to quantify this with certainty. However, based on these numbers, it is reasonable to assume that the actual numerical uncertainty is at least within 4%–5% for both C_L and C_D at the selected refinement level. The low uncertainty estimates, along with the minimal differences in results between cases of significantly different cell counts presented in Figs. 22 and 23, indicate that we have reliable 3D RANS results of sufficiently fine resolution to yield only minor differences with further refinement.

Due to the limitations of available computational resources, it is not feasible to conduct separate studies on the numerical uncertainty for each of the four geometries discussed in Section 3. It is expected that the numerical uncertainty may slightly increase with the introduction of a free surface.

The high aspect ratio of the NTNU HFF1 main hydrofoil leads to significantly larger mesh sizes for the same chordwise resolution, as compared to the geometries studied in Sections 3.1 and 3.2. Since this was also studied in wave cases, for which long simulation times are needed to get converged results, using the same resolution as above would lead to excessive requirements for CPU time. Therefore, we have slightly increased the cell sizes to $h_{ref} = 2^{5/6} \times 10^{-3}$ for the NTNU HFF1 geometry. In order to preserve the details around the sharp trailing edge, a cylindrical refinement zone has been introduced around it. The refinement zone has a diameter of 7.5% of the average chord length and an internal cell size of $0.5 \times h_{ref}$. Apart from these adjustments, all other settings remain consistent with the ones described earlier. The total cell count for these simulations amounts to 83.9 million.

A.3. Visualization of 3D RANS results

To provide an overview of the simulation domain and the physics at hand, we have chosen to include visualizations of an example of results from the 3D RANS simulations herein. These are all made from the case of the NTNU HFF1 main hydrofoil operating in calm water conditions at 0° angle of attack.

Fig. 24 illustrates the flow and pressure fields resulting from the calm water simulation of the NTNU HFF1 main hydrofoil. Figs. 24(a) and 24(b) show streamlines and cut planes coloured by the dynamic pressure and a cut plane coloured by the flow speed, respectively. Fig. 24(c) shows a top view of the computational domain which has been colour coded by the wave elevation.

Appendix B. 2D models

With all force predictions originating from 2D lift and drag models, the choice of how to create these is naturally a key element of obtaining accurate results from the NDLL. The models are based on the creation and interpolation of datasets for C_L, C_D, and pressure distributions, and require simulations from which these parameters can be extracted. Our main focus is high-Reynolds-number applications, and a key part of our verification and validation study is centred around comparison with 3D RANS simulations. The latter implicitly assumes a fully turbulent flow. It is hence reasonable to use 2D models with similar assumptions, ideally originating from RANS simulations with a similar setup.

One alternative would be to run 2D RANS using the same software and meshing, schemes, and solver settings as used in 3D RANS. This would minimize modelling differences between the 2D data and reference data, isolating the uncertainties from the NDLL formulation itself. Doing so did however yield challenges in the form of irregularities of 2D results between very similar cases. Extensive investigations have revealed that result scatter mainly originates from the applied meshing software, snappyHexMesh, not being able to consistently reconstruct

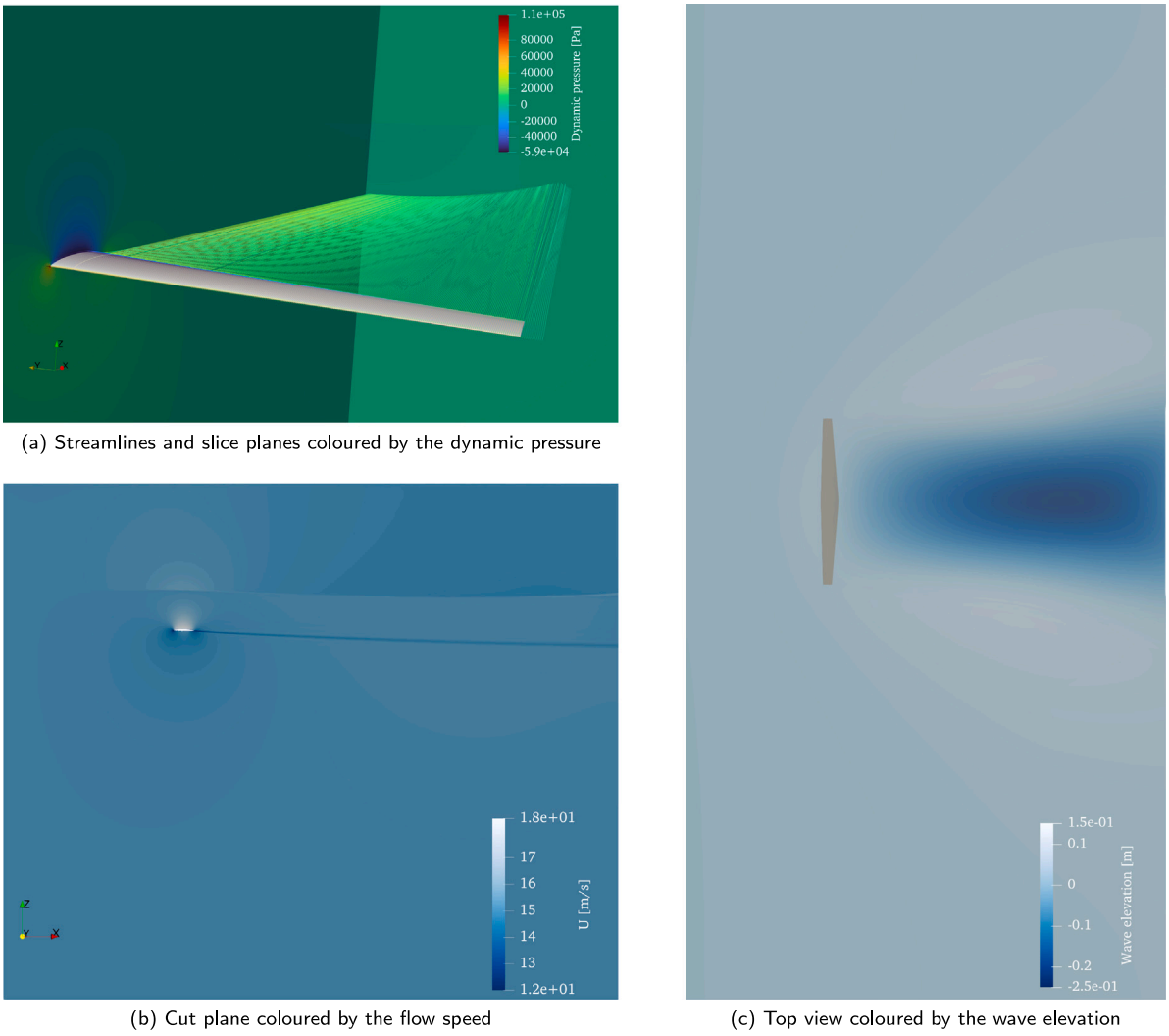

(a) Streamlines and slice planes coloured by the dynamic pressure

(b) Cut plane coloured by the flow speed

(c) Top view coloured by the wave elevation

Fig. 24. Visualizations of the NTNU HFF1 main hydrofoil operating in calm water at 0° angle of attack.

the geometry accurately in cases with near-wall prism layers and chordwise varying refinement. In some cases, there is also scatter due to inconsistencies in prism-layer generation. The mesher is an unstructured-grid generator, and there is no practical way to a priori predict when these problems occur. In 3D simulations, the impact on results is small, since the problems typically only affect a small portion of the span.

To mitigate the scatter in 2D results, an alternative would be to simulate constant-profile sections spanning the entire width of relatively narrow 3D simulation domains. However, this approach significantly increases mesh sizes and computational time required to generate 2D models. Consequently, we opted for a fundamentally different meshing approach for the 2D models using the blockMesh utility in OpenFOAM, which generates structured meshes. This eliminates the aforementioned issues, but it may introduce systematic differences in C_L and C_D predictions due to meshing-related issues in the 3D RANS simulations that are absent in the 2D RANS simulations. One example of such issues is the existence of a strict limitation on the possible number of prism layers and the dimension of the widest of these relative to non-prism-layer cells, to avoid inconsistent layer generation. This leads to a step in cell size within the boundary layer, at the transition between prism-layer cells and adjacent cells. Other sources include local coarsening of the cross-flow resolution in the region of prism-layer collapse and systematic irregularities in geometry representation in the 3D RANS simulations.

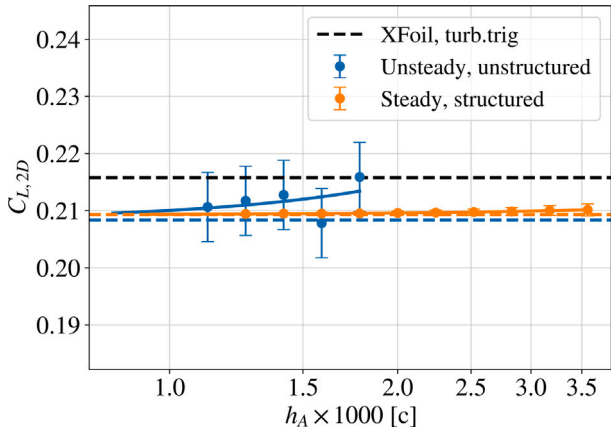

Fig. 25. Comparison of convergence paths of $C_{L,2D}$ with mesh refinement, from unstructured and structured grids. XFOIL data with triggered turbulence at 5% chord is included for reference. All results are for NACA23012 at Re $= 8.16 \times 10^6$.

Figs. 25 and 26 compare the convergence paths of 2D models based on unsteady simulations with unstructured grids and those from steady simulations on structured grids. The latter converges towards C_L and C_D values which are 0.5% and 3.2% higher than those of the former.

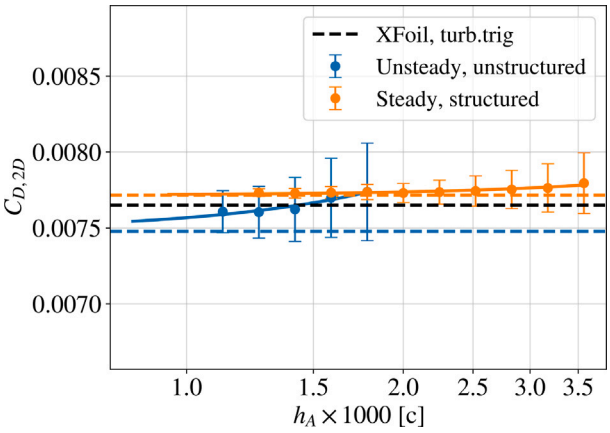

Fig. 26. Comparison of convergence paths of $C_{D,2D}$ with mesh refinement, from unstructured and structured grids. XFOIL data with triggered turbulence at 5% chord is included for reference. All results are for NACA23012 at $\mathrm{Re} = 8.16 \times 10^6$.

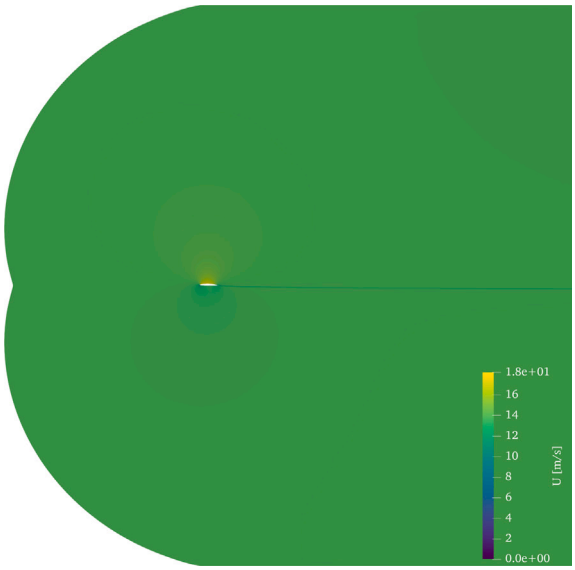

Fig. 27. Results from one of the simulations that were used to create the 2D models herein.

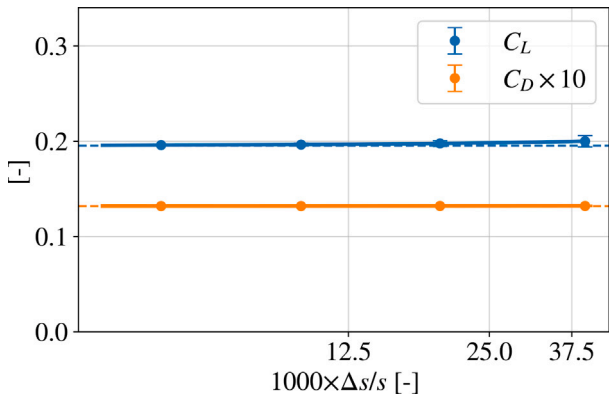

Fig. 28. C_L and C_D as a function of the spanwise length of the bound line elements relative to wing span.

Since our 3D RANS reference data is created with unsteady simulations on unstructured grids, we expect systematic differences between profile properties in this relative to the profile models used in the NDLL. The latter are generated by steady simulations on structured grids. This does not mean the NDLL is less accurate, there is rather a chance the profile data for this is more accurate than that in 3D RANS. The fact that it converges to values which are closer to those predicted by XFOIL supports this hypothesis. However, it means that slightly higher predictions of forces, especially drag, are expected from NDLL than from 3D RANS.

B.1. Applied settings in 2D models

All 2D models used in Section 3 were created with structured meshes, $h_A = 2 \times 10^{-3} c$ and a steady solver. Steps of 0.5° and 0.01 were applied in the angle of attack α and relative camber height, respectively. The numerical uncertainty is then predicted as 0.4% and 0.8% for $C_{L,2D}$ and $C_{D,2D}$, respectively.

The case study in Section 5 required a wide range of angles of attack, flap angles, and Reynolds numbers, the latter due to different chord lengths of main and tail hydrofoils. To reduce the number of simulations needed, we applied coarser steps of 2° for $|\alpha| \leq 8°$, steps of 4° for $8° < |\alpha| \leq 12°$, and steps of 8° for angles outside these ranges. α_f was equivalently incremented by 2° for $|\alpha_f| \leq 8°$, and by 8° outside this range. Relative camber height was incremented by 0.03. Even with this coarser stepping of geometrical properties, a total of 714 2D RANS simulations had to be conducted to construct the interpolation model. A slightly coarser mesh resolution, corresponding to $h_A = 2^{3/2} \times 10^{-3} c$, was used in these 2D simulations.

B.2. Visualization of 2D RANS results

It is judged reasonable to include a visualization of one of the simulations that were used in the creation of the 2D models herein. Fig. 27 shows the computational domain for such a simulation, colour coded by the flow speed. The case at hand is a profile of NACA66-010 thickness distribution and NACA a=0.8(modified) camber line, with an angle of attack of 2° and a camber ratio of 0.03, operating at a Reynolds number of 12×10^6.

Appendix C. Numerical uncertainty of NDLL simulations

The numerical uncertainty of NDLL simulations consists of two types of contributions: those originating from the lifting line formulation itself, or the outer domain, and those originating from the numerical uncertainty in the 2D models. The latter is treated separately in Appendix B.

We estimate the numerical uncertainty of the outer domain by repeated simulations with varying spanwise resolutions. Fig. 28 shows the results of repeated simulations of the geometry used by Wadlin et al. (1955), detailed in Table 2. Δs denotes the length of the bound line elements and ranges from $\frac{1}{25}$ s to $\frac{1}{201}$ s. We estimate numerical uncertainty by the procedure of Richardson extrapolation, following the guidelines for "Estimating errors and uncertainties using a least squares root approach" for CFD simulations by the 28th ITTC Resistance Committee (2017). With 101 spanwise elements, this yields numerical uncertainties of 1.57×10^{-3} and 1.41×10^{-5} C_L and C_D, respectively. This corresponds to 0.8% and 0.1% of nominal values for this case. All simulations herein have been performed with 101 or more spanwise elements.

We assume uncertainty from the inner and outer domains to combine as a root sum of squares, presented in Eq. (25). This is equivalent to the way uncertainty from subcomponents is combined in the procedures of the 28th ITTC Resistance Committee (2017). $U_{M,tot}$ denotes the total uncertainty of the model, U_i denotes the uncertainty of subcomponent i, and N denotes the total number of uncertainty components. Combining uncertainties from the outer and inner components of the

NDLL formulation hence yields total uncertainty estimates of $U_{C_L} = 0.9\%$ and $U_{C_D} = 0.8\%$.

$$U_{M,tot} = \sqrt{\sum_{i=1}^{N} U_i} \tag{25}$$

C.1. Validation limits

Referring again to the 28th ITTC Resistance Committee (2017), we consider simulation results validated at the U_V level they correspond within the validation uncertainty U_V, as defined in Eq. (26). U_D denotes the uncertainty of the reference data.

$$U_V = \sqrt{U_D^2 + U_{M,tot}^2} \tag{26}$$

Quantitative values of uncertainty are not available for the experiments used in the validation procedures herein. Referring to discussions in Section 3.3 it is judged highly likely that the correspondence is within U_V for all investigated experimental cases.

When comparing NDLL and 3D RANS, we can estimate the validation uncertainty by using the numerical uncertainty of 3D RANS U_D. Referring to the discussions in Appendix A, we can only make a rough estimate of the latter, of 4%–5% of nominal values. This yields validation uncertainties in the range of 4.1% to 5.1% for C_L and C_D. These values are to be seen as estimates. They are based on a limited number of test cases and are likely to vary with geometry and operating conditions. The percentage uncertainty of C_L will also naturally spike close to $C_L = 0$.

Since both NDLL and RANS results originate from simulations, discrepancies between the two are not necessarily attributed to the NDLL. In addition to the numerical uncertainties discussed here, it is worth mentioning that the 2D models were generated for a wide range of Reynolds numbers, adjusting layering settings to achieve the same y^+ and close to the same layer expansion in each. The 3D RANS was performed with uniform layering settings across the hydrofoil, meaning the inner cell height is constant and y^+ varies with local chord length. There are hence significant local differences in y^+ and the number of prism layers between the simulations used for constructing 2D models for the NDLL and the 3D RANS simulations. This might increase the discrepancies between NDLL and 3D RANS, in the form of the profile properties in the latter being predicted in a more simplified way.

Appendix D. NDLL settings

Section 2 presents the theoretical foundation of the Non-Linear Dynamic Lifting Line (NDLL) method herein. This includes a series of adjustable parameters. To ensure reproducibility, we present the specific settings applied in Sections 3 and 5 in Table 4. In the table, ΔT represents the time step, and C.W. and W. indicate calm water and wave conditions, respectively.

δ_{vc} was set to 0.25 in the NTNU HFF1 cases, as this yielded better correspondence of wake velocity data with those from 3D RANS, as compared to the original value of 1.0 used in other cases. Re-running the NTNU HFF1 calm water case at $\alpha = 0$ with $\delta_{vc} = 1.0$ resulted in a negligible 0.001% change of C_L and C_D. This indicates that the modified viscous core tuning parameter did not significantly impact the force results.

The results of Appendix C indicate that practically no effect is expected from the different numbers of spanwise elements used in different cases. A slightly shorter wake was used in the Wadlin case, as compared to other cases. The effect of this was quantified in Section 3.2.1.

Appendix E. NTNU HFF1

Significant changes have occurred in the field of hydrofoil fast ferry design since its last period of commercial application. Previous vessels like the Boeing Jetfoil (Feifel, 1981), Kværner Fjellstrand Foilcat Jorde (1991) and Minsaas (1993), and Westamarin Foilcat 2900 (Svenneby and Minsaas, 1992) featured canard-configured foil systems and achieved top speeds around 50 knots. However, present-day design companies such as Artemis Technologies (Artemis Technologies, 2022), Candela (Candela, 2022), Boundary Layer Technologies (Boundary Layer Technologies, 2022), and Glosten/Bieker Boats (Bieker Boats, 2022) are focused on maximizing energy efficiency to increase the range of zero-emission vessels. As a result, the design speeds have been lowered to a range of 25 to 38 knots. The typical foil layout now follows the “aeroplane” or “conventional” configuration (Johnston, 1985), featuring a main lifting hydrofoil positioned near the longitudinal centre of gravity and one or two tail hydrofoils for pitch and yaw stability. All the mentioned designs utilize fully submerged hydrofoil systems, with no lifting surfaces piercing the water surface. The exact design details of these companies’ vessels have not been publicly disclosed.

For the purposes of this study and future investigations into hydrofoil vessels, it is deemed reasonable to analyse a hydrofoil system that represents modern hydrofoiling fast ferry concepts. Hence, we have developed a hydrofoil system called the NTNU Hydrofoiling Fast Ferry 1 (NTNU HFF1), combining available information with a design philosophy based on well-established principles of hydrodynamics and dynamic stability analyses. The geometry of the NTNU HFF1 has been published online to facilitate its use in future studies (Godø and Steen, 2023). In this section, we outline the hydrofoil design method and present the major assumptions that have been made in the design process.

It is important to note that the current work primarily focuses on hydrodynamic simulation methods. While there are numerous other challenges involved in hydrofoil design beyond creating an optimized hydrodynamic shape, we have chosen to narrow our focus to this aspect. Mechanical challenges such as hydrofoil installation methods in the hull or the evaluation of structural rigidity and ultimate strength, which should be assessed for collision or dynamic load scenarios, are not evaluated in this study. Similarly, the design of a propulsion system is beyond the scope of our analysis.

E.1. Size, weight, and speed

Table 5 presents key data on the main dimensions, mass, and speed of the NTNU HFF1. In the table, L_{OA}, B, M, r_{xx}, r_{yy}, and $Fn_{h,design}$ denote the length overall, breadth overall, vessel mass, roll radius of inertia, pitch radius of inertia, and the submergence Froude number at design speed, respectively.

E.2. Hydrofoil layout

The NTNU HFF1 incorporates a main lifting hydrofoil positioned near the longitudinal centre of gravity, accompanied by a single tail hydrofoil. The single-tail configuration is chosen to avoid large spanwise inflow variations to twin tails caused by tip vortices passing in their proximity, as illustrated in Fig. 14. Both the main and tail hydrofoils feature a taper ratio of 0.5. Struts and junction boxes between struts and hydrofoils are left out of the current geometry. This is to avoid the introduction of errors from junction drag correction factors, as well as to reduce the computational load in the RANS-based validation in Section 3.3. The planform of the NTNU HFF1 is illustrated as seen from above in Fig. 29. The subsequent sections present the details of the design.

Table 4
NDLL settings applied in Sections 3 and 5.

	J & C	Wadlin	Wilson	HFF1 C.W.	HFF1 W.	Case study
Spanwise elements	201	201	101	101	101	41
$U\Delta T/c_{mean}$	0.29	0.29	0.29	0.19	0.19	0.31
Wake length [c_{mean}]	15	15	10	15	15	10
GF downsampling factor	N.A.	4	4	8	8	4
δ_{vc}	1.0	1.0	1.0	0.25	0.25	1.0

Table 5
Main dimensions and weight of NTNU HFF1.

Parameter	Value
L_{OA} [m]	24
B	11.0
Foil submergence at speed [m]	2
M [kg]	60 000
r_{xx}/B	0.33
r_{yy}/L_{OA}	0.33
Design speed [knots]	35
Max speed [knots]	38
$Fn_{h,design}$ [−]	4.06
Main hydrofoil x pos., rel. to CG [m]	−1.1
Main hydrofoil span [m]	11
Main hydrofoil aspect ratio [−]	12.3
Main hydrofoil midspan chord [m]	1.19
Main hydrofoil taper ratio [−]	0.5
Main hydrofoil max camber [% chord]	2.5
Main hydrofoil thickness distribution	NACA 66−010
Main hydrofoil camber line	NACA a = 0.8 (mod)

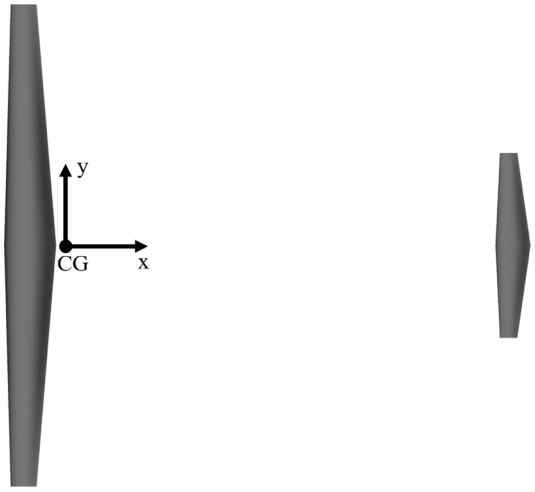

Fig. 29. Planform of the NTNU HFF1 hydrofoil design, as seen from above. The centre of gravity is marked as CG, and × points towards the aft of the vessel.

E.3. Foil section and cavitation considerations

Faltinsen (2005) notes that a certain extent of leading-edge cavitation must be tolerated when operating a hydrofoil vessel in a seaway, while cavitation originating close to the mid-chord should be avoided. To maximize lift within the pressure-drop limit imposed by cavitation constraints, it is desirable to have a foil section with a relatively flat chordwise pressure distribution. Furthermore, Faltinsen points out that care must be taken to avoid a pronounced suction peak at the longitudinal position of the flap.

In our design, we utilize the NACA 66 − 010 thickness distribution combined with the NACA $a = 0.8$ (modified) camber line. These choices result in relatively flat chordwise pressure distributions. A 2D model is created using the FASTSHIPS 2D model module, which is fed by a set of 2D RANS simulations conducted at various camber heights, Reynolds numbers, angles of attack, and flap angles. This module extracts lift, drag, and pressure distribution data, and creates interpolation models for each parameter.

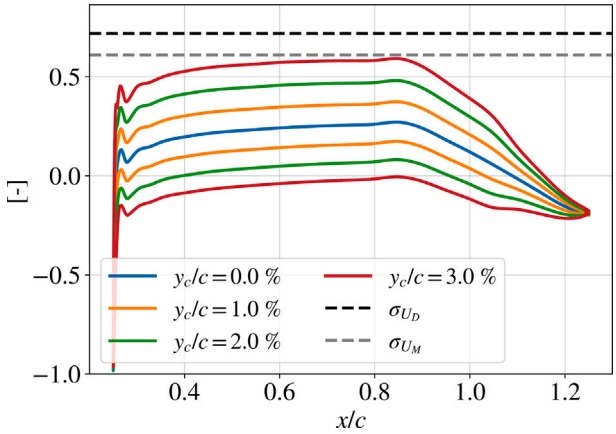

Fig. 30. $-C_p$ and σ for NACA 66−010 + NACA a = 0.8(modified) sections at twice the ideal angle of attack, as predicted by the FASTSHIPS 2D model for Reynolds number 5.0e6. Black and grey dashed lines indicate the cavitation number σ at design speed and max speed, respectively.

Fig. 30 depicts the $-Cp$ distribution for the combined thickness and camber distribution at camber heights ranging from 0 to 3%. Here, C_p is defined by Eq. (27), and y_c denotes the camber height. The cavitation number σ is indicated by dashed lines. σ is defined in Eq. (28), with $p_0 = p_{atm} + \rho g z$ and p_v denoting the vapour pressure of water. The latter is assumed to be 2000 Pa in Fig. 30. The cavitation numbers at design speed and maximum speed are denoted as σ_{U_D} and σ_{U_M}, respectively. The figure shows results for a Reynolds number of Re = 5.0e6, corresponding to a 50% scale of the NTNU HFF1. The angle of attack has been adjusted to twice the ideal angle of attack as given by Abbott and von Doenhoff (1959), introducing a slight contribution to lift from the angle of attack. This adjustment flattens the chordwise pressure curve and allows for higher C_L values before cavitation inception.

$$C_p = \frac{p - p_0}{0.5\rho U^2} \tag{27}$$

$$\sigma = \frac{p_0 - p_v}{0.5\rho U^2} \tag{28}$$

The design of local foil sections commences with a cavitation assessment based on Fig. 30, which determines the maximum permissible camber that avoids cavitation at the desired angle of attack. We choose a maximum camber limit of 2.5% chord, allowing for a slight margin against cavitation at max speed. The hydrofoil span, spanwise distribution of bound circulation, and the spanwise variation of relative chord length are treated as predetermined parameters. This allows the calculation of the relative variation of C_L along the span. The magnitude of the C_L values, and hence the maximum C_L value, are now a function of the scaling of the chord length distribution. We scale it such that the spanwise C_L distribution reaches its peak at the maximum value derived from the cavitation constraint. Subsequently, we employ the 2D model from FASTSHIPS to identify the corresponding distribution of camber height. As for the circulation distribution, this is set as the bell

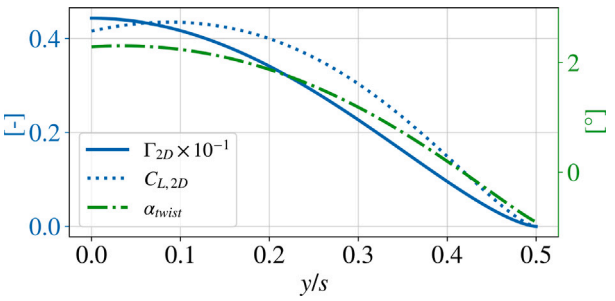

Fig. 31. Spanwise distributions of twist angle α_{twist}, 2D lift coefficient $C_{L,2D}$, and 2D circulation Γ_{2D} of the NTNU HFF1 main hydrofoil.

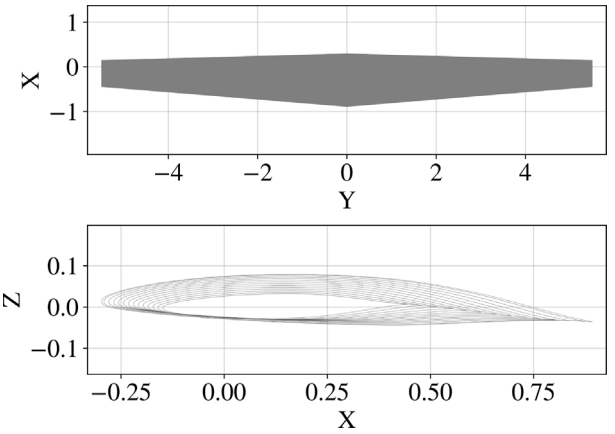

Fig. 32. Top and side views of the NTNU HFF1 main hydrofoil.

distribution. This circulation distribution has been shown to yield the minimum induced drag within bending-moment constraints on aircraft wings (Prandtl, 1933), while providing smooth variations of lift coefficients and downwash/upwash at the wing tips, and having beneficial manoeuvring characteristics in the form of proverse yaw (Bowers et al., 2016).

With the spanwise variation of chord length and camber established, the final design step involves determining the local twist angles. To accomplish this, we run the NDLL with the circulation distribution forced to the target distribution, allowing us to extract local inflow angles along the span of the hydrofoil. The simulation accounts for the full 3D solution from the NDLL, including wake deformation, tip vortex roll-up, free surface gravity waves, and hydrofoil interaction. The twist angles are then set so that each section operates at twice its ideal angle of attack, in accordance with the values employed in the cavitation assessment. The resulting spanwise variations of twist angle α_{twist}, 2D lift coefficient $C_{L,2D}$, and circulation per unit span Γ_{2D} are depicted in Fig. 31. The shape of the hydrofoil is shown in Fig. 32, while key data are provided in Table 5.

E.3.1. Flap design

Pressure recovery starts at approximately 60% chord for the thickness distribution and at 80% chord for the camber line. We assume hinged flaps with the rotation centre at the mean line at the 75% chord position. This places the hinge slightly downstream of the chordwise start of pressure recovery for the profile, providing an additional pressure margin against cavitation in the vicinity of the low-pressure peak at the flap hinge.

The flap comprises the exposed foil profile aft of 75% chord and a concealed circular-arc section within the foil profile at zero deflection. If the upstream non-flap profile consisted only of the outer geometry and a circular arc section, flap deflection would be physically

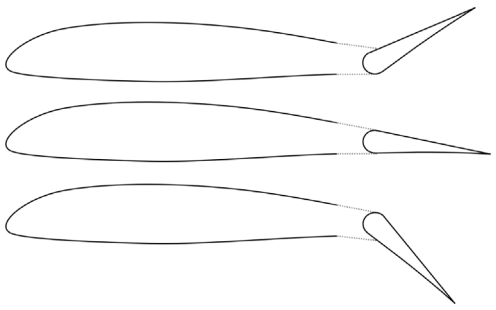

Fig. 33. Flap design of the NTNU HFF1. The grey parts represent fairings which deflect to allow for a vertical offset of the intersection point between the forward and aft parts. Flap deflection amplitudes are exaggerated for illustration purposes.

impossible, as an immediate collision would occur between the two parts on the concave side. Additionally, a dent would appear on the convex side where the circular arc was exposed. To enhance realism, we model the upstream section as a rigid section with deflectable fairing sections in the aftmost 5% chord region. When deflecting the flap, the fairings deflect outwards on both sides. On the concave side, the fairing allows the flap to deflect without crashing into the rigid parts of the upstream foil section. On the convex side, it merges the upstream section with the now exposed circular arc of the flap. Fig. 33 illustrates this arrangement, with the fairings depicted in grey colour.

The NTNU HFF1 is equipped with three flaps. The main hydrofoil features one flap near each end of the span, ranging from $y/s_{main} = \pm 0.125$ to $y/s_{main} = \pm 0.49$. Here, s_{main} denotes the span of the main hydrofoil. These provide control authority for both roll and heave, resembling "flaperons" in aircraft terminology. The third flap is located at the tail hydrofoil, spanning from $y/s_{tail} = -0.49$ to $y/s_{tail} = 0.49$. Here, s_{tail} denotes the span of the tail hydrofoil. Acting similarly to the elevator of an aircraft, this flap primarily actuates the pitch of the vessel.

E.4. Tail sizing for passive pitch stability

Johnston (1985) defines a hydrofoil layout as *conventional* if the aft hydrofoil(-s) support 0%–35% of the weight of the vessel. In any hydrofoil configuration, the aft hydrofoil operates in the downwash of the forward. This tilts the lift vector backwards and hence has an adverse impact on its ratio of lift to drag. Free surface gravity waves might partly cancel this effect at certain combinations of longitudinal spacing and vessel speeds (Mørch, 1992). However, experimentation with different designs in the current simulation model indicates that a net downwards inflow is typically present at the tail at realistic combinations of hydrofoil spacing and design speed. A consequence of this is that the hydrofoil designer in search of energy-efficient designs would aim to minimize the ratio of tail lift to total lift.

On the other hand, safety considerations might yield a desire to have a slightly positive tail lift in a design condition. This is to avoid a net negative tail lift in cases with off-design longitudinal CG position. A negative tail lift could result in a nose dive in the case of tail ventilation. Therefore, we assume a positive tail lift equivalent to 10% of the vessel's weight. For the 24 m long NTNU HFF1, we assume the centre of gravity to be positioned approximately 10 m from the stern, allowing a tail placement 10 m aft of CG. This implies that the main hydrofoil must be placed 1.1 m in front of CG to balance the pitch moment from the tail at the design condition.

Fossen (1994) provides an expression for the inherent pitch stability of hydrofoil vessels, given by Eq. (29). In this equation, C_{L0} represents the mean lift coefficient, and $C_{L\alpha}$ denotes the lift coefficient per unit angle of attack. In practical terms, this states that the restoring spring coefficient in pitch about CG, assuming an uncoupled system and small

Table 6
Tail hydrofoil design requirements and dimensions of NTNU HFF1.

Parameter	Value
Λ [−]	7
Tail hydrofoil x pos.rel. to CG [m]	10.0
A [m^2]	2.55
Taper ratio [−]	0.5
Relative untapered span	25%
Thickness distribution	NACA 66−010
Camber line	NACA a = 0.8 (mod)

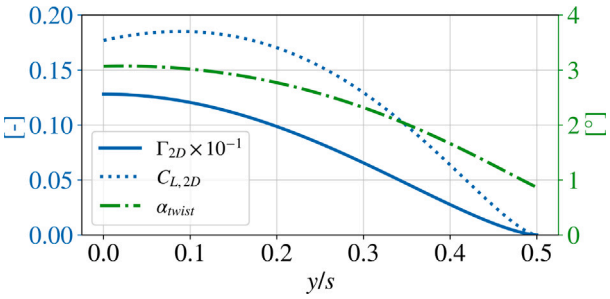

Fig. 34. Spanwise distributions of twist angle α_{twist}, 2D lift coefficient $C_{L,2D}$, and 2D circulation Γ_{2D} of the NTNU HFF1 tail hydrofoil.

pitch angles, is to be positive. We assume the three-dimensional lift coefficient slope to be determined by Eq. (20) (Faltinsen, 2005), and the aft hydrofoil to have an aspect ratio of 7. Λ denotes the aspect ratio. To allow longitudinal load shifts without compromising safety, we require a positive spring constant with a 1.0 m aft shift of CG. We can now calculate the minimum tail hydrofoil area from pitch stability considerations. Table 6 presents the key data for the resulting hydrofoil. We have simplified our analysis by neglecting the effect of free surface proximity on lift slopes when evaluating pitch stability. This is a conservative simplification, since the forward hydrofoil with the larger chord length will experience the largest reduction in lift slope at a certain absolute depth, thereby increasing the restoring spring coefficient in pitch relative to that predicted by our approach.

$$\left(\frac{C_{L\alpha}}{C_{L0}}\right)_{fore} < \left(\frac{C_{L\alpha}}{C_{L0}}\right)_{aft} \tag{29}$$

The open-loop uncoupled pitch motion can be described by Eq. (30). In this equation, I_y represents the pitch moment of inertia, M_y denotes the pitch moment, and θ represents the pitch angle. Derivatives are denoted by dots, and we neglect the effect of added mass forces. The derivatives $\frac{\delta M_y}{\delta \dot{\theta}}$ and $\frac{\delta M_y}{\delta \theta}$ are defined in Eqs. (31) and (32), respectively. The longitudinal positions of the fore and aft hydrofoils relative to the centre of gravity (CG) are denoted as x_{fore} and x_{aft}, respectively. The pitch moment of inertia is found as $I_y = M \times (r_{yy} L_{OA})^2$, and we can now solve the linear mass–damper–spring system equations. This yields a relative damping ratio of 1.0 and a natural pitch oscillation period of 3.4 s.

$$I_y \ddot{\theta} + \frac{\delta M_y}{\dot{\theta}} \dot{\theta} + \frac{\delta M_y}{\delta \theta} \theta = 0 \tag{30}$$

$$\frac{\delta M_y}{\delta \dot{\theta}} = 0.5 \rho U^2 \left(\frac{C_{L\alpha,fore} x_{fore}^2}{U} + \frac{C_{L\alpha,aft} x_{aft}^2}{U} \right) \tag{31}$$

$$\frac{\delta M_y}{\delta \theta} = 0.5 \rho U^2 (C_{L\alpha,fore} x_{fore} + C_{L\alpha,fore} x_{fore}) \tag{32}$$

Once the mean lift, planform, and area are determined, we can calculate the spanwise distribution of circulation and the 2D lift coefficient of the tail hydrofoil. Similar to the main hydrofoil, we assume a bell-shaped spanwise circulation distribution and adjust the twist angle so that the foil sections operate at twice the ideal angle of attack. Inflow angles are determined by the use of the NDLL while forcing circulation to the desired distribution, taking into account the interaction with the wake and gravity waves generated by the upstream hydrofoil. The resulting values of circulation, lift coefficient, and twist angle are depicted in Fig. 34. The three-dimensional geometry of the NTNU HFF1 hydrofoils can be found as Wavefront (.obj) files and as tabulated data on the spanwise variation of camber, thickness, twist angle, and chord length, at the FASTSHIPS website (Godø and Steen, 2023).

References

28th ITTC Resistance Committee, 2017. Uncertainty Analysis in CFD Verification and Validation, Methodology and Procedures. Technical Report, International Towing-Tank Conference (ITTC).

Abbott, I.H., von Doenhoff, A.E., 1959. Theory of Wing Sections: Including a Summary of Airfoil Data. Dover Publications Inc..

Anderson, R.F., 1938. The Experimental and Calculated Characteristics of 22 Tapered Wings. Technical Report, NACA Technical Rerport No. 627, National Advisory Committee for Aeronautics.

Artemis Technologies, 2022. EF-24 passenger. URL https://www.artemistechnologies.co.uk/ef-24-passenger-ferry/.

Balduzzi, F., Marten, D., Bianchini, A., Drofelnik, J., Ferrari, L., Campobasso, M.S., Pechlivanoglou, G., Nayeri, C.N., Ferrara, G., Paschereit, C.O., 2018. Three-dimensional aerodynamic analysis of a darrieus wind turbine blade using computational fluid dynamics and lifting line theory. J. Eng. Gas Turbines Power.

Bieker Boats, 2022. Foiling fast ferry. URL https://biekerboats.com/project/foiling-fast-ferry/.

Bøckmann, E., 2015. Wave Propulsion of Ships (Ph.D. thesis). Norwegian University of Science and Technology.

Bøckmann, E., Steen, S., 2013. The effect of a fixed foil on ship propulsion and motions. In: Third International Symposium of Marine Propulsors. Tasmania, Australia.

Bøckmann, E., Steen, S., 2016. Model test and simulation of a ship with wavefoils. Appl. Ocean Res..

Boundary Layer Technologies, 2022. Electra. URL https://www.boundarylayer.tech/electra.

Bowers, A.H., Murillo, O.J., Jensen, R.R., Eslinger, B., Gelzer, C., 2016. On Wings of the Minimum Induced Drag: Spanload Implications for Aircraft and Birds. NASA Technical Publication - 2016 - 219072. Technical Report, NASA.

Bullivant, W.K., 1941. Tets of the NACA 0025 and 0035 Airfoils in the Full-Scale Wind Tunnel. Technical Report, NACA Technical Report No. 708, National Advisory Committee for Aeronautics.

Candela, 2022. P12 Shuttle. URL https://candela.com/p-12-shuttle/.

Carter, D.J.T., 1982. Prediction of wave height and period for a constant wind velocity using the JONSWAP results. Ocean Eng..

Duport, C., Deberque, M., Leroux, J.B., Roncin, K., Jochum, C., 2017. Local results verification of a 3D non-linear lifting line method for fluid-structure interactions simulation on a towing kite for vessels. In: High-Performance Marine Vehicles.

Duport, C., Leroux, J.B., Roncin, K., Jochum, C., Parlier, Y., 2016. Comparison of 3D non-linear lifting line method calculations with 3D RANSE simulations and application to the prediction of the global loading on a cornering kite. In: Proceedings of the 15th Journées de L'Hydrodynamique.

Eastman, N.J., Ward, K.E., Pinkerton, R.M., 1935. The Characteristics of 78 Related Airfoil Sections from Tests in the Variable-Density Wind Tunnel. Technical Report, NACA Technical Report No. 460, National Advisory Committee for Aeronautics.

Epps, B., 2010. OpenProp v2.4 Theory Document. Technical Report, Massachusets Institute of Technology.

Epps, B., Chalfant, J., Kimball, R., Techet, A., Flood, K., Chryssostomidis, C., 2009. OpenProp: An open-source parametric design and analysis tool for propellers. In: Proceedings of the 2009 Grand Challenges in Modeling and Simulation Conference.

Epps, B.P., Kimball, R.W., 2013. Unified rotor lifting line theory. J. Ship Res..

Epps, B., Víquez, O., Chryssostomidis, C., 2011. Dual-operating-point blade optimization for high-speed propellers. In: 11th International Conference on Fast Sea Transportation, FAST.

Falch, S., 1991a. Seakeeping of foilcatamarans. In: 1st International Conference on Fast Sea Transportation (FAST).

Falch, S., 1991b. Sjøegenskaper for Foilkatamaraner. Technical Report, Norsk Marinteknisk Forskningsinstitutt, MARINTEK.

Faltinsen, O.M., 1990. Sea Loads on Ships and Offshore Structures. Cambridge University Press.

Faltinsen, O.M., 2005. Hydrodynamics of High-SPeed Marine Vehicles. Cambridge University Press.

Feifel, W.M., 1981. Advanced numerical methods hydrofoil system design and experimental verification. In: Third International Conference on Numerical Ship Hydrodynamics.

Findlay, M.W., Turnock, S.R., 2008a. Development and use of a velocity prediction program to compare the effects of changes to foil arrangement on a hydrofoiling moth dinghy. In: International Conference on Innovation in High Performance Sailing Yachts, INNOV'sAIL.

Findlay, M.W., Turnock, S.R., 2008b. Investigating sailing styles and boat set-up on the performance of a hydrofoiling moth dinghy. In: 20th International HISWA Symposium on Yacht Design and Yacht Construction.
Fossen, T.I., 1991. Nonlinear Modeling and Control of Underwater Vehicles (Ph.D. thesis). Norwegian University of Science and Technology.
Fossen, T.I., 1994. Guidance and Control of Ocean Vehicles. John Wiley & Sons Ltd..
Fossen, T.I., 2011. Handbook of Marine Craft Hydrodynamics and Motion Control. John Wiley & Sons Ltd..
Godø, J.M.K., Kramer, J.V., Steen, S., Savio, L., 2018. Unsteady forces on hydrofoil vessels in waves - validation of a dynamic lifting line using CFD. In: 21st Numerical Towing Tank Symposium.
Godø, J.M., Steen, S., 2023. FASTSHIPS. URL https://www.ntnu.edu/imt/software/fastships.
Goett, H.J., Bullivant, W.K., 1938. Tests of NACA 0009, 0012 and 0018 Airfoils in the Full-Scale Tunnel. Technical Report, NACA Technical Report No. 647, National Advisory Committee for Aeronautics.
Graf, K., Hoeve, A., Watin, S., 2014. Comparison of full 3D-RANS simulations with 2D-RANS/lifting line method calculations for the flow analysis of rigid wings for high performance multihulls. Ocean Eng..
Grasso, F., van Garrel, A., Schepers, J.G., 2011. Development and validation of generalized lifting line based code for wind turbine aerodynamics. In: 49th AIAA Aerospace Sciences Meeting, 30th ASME Wind Energy Symposium.
Hally, D., 1994. Integration of the Wave Resistance Green Functions Over Planar Panels. Technical Report, Defence Research Establishment Atlantic.
Hoerner, S.F., 1965. Fluid-Dynamic Drag. Hoerner, S. F..
Hunsaker, D.F., 2011. A numerical lifting-line method using horseshoe vortex sheets. In: Utah Space Grant.
Jacobs, E.N., Abbott, I.H., 1933. The NACA Variable-Density Wind Tunnel. Technical Report, NACA Technical Report No. 416, National Advisory Committee for Aeronautics.
Jacobs, E.N., Clay, W.C., 1936. Characteristics of the NACA 23012 Airfoil from Tests in the Full-Scale and Variable-Density Tunnels. Technical Report, NACA Technical Report No. 530, National Advisory Committee for Aeronautics.
Jacobs, E.N., Ward, K.E., Pinkerton, R.M., 1935. The Characteristics of 78 Related Airfoil Sections from Tests in the Variable-Density Wind Tunnel. Technical Report, NACA Technical Report No. 460, National Advisory Committee for Aeronautics.
Johnston, R.J., 1985. Hydrofoils.
Jorde, J.H., 1991. The development of a 50 knot 40 m foilcat. In: Proceedings of the 1st International Conference on Fast Sea Transportation.
Katz, J., Plotkin, A., 2001. Low-Speed Aerodynamics. Cambridge University Press.
Keuning, J.A., 1979. A calculation method for the heave and pitch motions of a hydrofoil boat in waves. Int. Shipbuild. Pprogress.
Kihara, K., Hamada, C., Miyoshi, M., Sueoka, H., Kawakami, T., Harada, T., Toki, N., 1993. Diesel driven fully submerged hydrofoil catamaran: Mitsubishi super-shuttle 400, the "RAINBOW". In: 2nd International Conference on Fast Sea Transportation, FAST.
Kramer, J.V.K., Godø, J.M.K., Steen, S., 2018. Hydrofoil simulations - non-linear lifting line vs CFD. In: Proceedings of the 21st Numerical Towing Tank Symposium.
Leishman, J.G., 2006. Principles of Helicopter Aerodynamics. Cambridge University Press,
Marten, D., Lennie, M., Pechlivanoglou, G., Nayeri, C.N., Paschereit, C.O., 2015. Implementation, optimization and validation of a nonlinear lifting line free vortex wake module within the wind turbine simulation code QBlade. In: ASME Turbo Expo 2015: Turbine Technical Conference and Exposition.
Marten, D., Lennie, M., Pechlivanoglou, G., Nayeri, C.N., Paschereit, C.O., 2016. Implementation, optimization and validation of a nonlinear lifting line-free vortex wake module withing the wind turbine simulation code QBlade. J. Eng. Gas Turbines Power.
Marten, D., Pechlivanoglou, G., Nayeri, C.N., Paschereit, C.O., 2018. Nonlinear lifting line theory applied to vertical axis wind turbines: development of a practical design tool. J. Fluids Eng..
Meyer, J.R., Wilkins, J.R.J., 1992. Hydrofoil development and applications. In: High Performance Marine Vehicles Conference and Exhibit.
Minsaas, K.J., 1993. Design and development of hydrofoil catamarans in Norway. In: Proceedings of the International Conference of Fast Sea Transportation.
Mørch, H.J.B., 1992. Aspects of Hydrofoil Design; with Emphasis on Hydrofoil Interaction in Calm Water (Ph.D. thesis). Norwegian University of Science and Technology.
Newman, J.N., 1977. Marine Hydrodynamics. MIT Press.
Ogilvie, T.F., 1959. The theoretical prediction of the longitudinal motions of hydrofoil craft. J. Ship Res..
Perić, R., Abdel-Maksoud, M., 2016. Reliable damping of free-surface waves in numerical simulations. Ship Technol. Res..
Phillips, W.F., Snyder, D.O., 2000. Modern adaptation of Prandtl's classic lifting-line theory. J. Aircr..
Platt, R.C., 1936. Turbulence Factors of NACA Wind Tunnels as Determined by Sphere Tests. Technical Report, NACA Technical Report No 558, National Advisory Committee for Aeronautics.
Prandtl, L., 1918. Tragflügeltheorie. Nachrichten Gesellschaft Wiss. Gött..
Prandtl, L., 1933. Über tragflügel kleinsten induzierten widerstandes. Z. Flugtecknik undMotorluftschiffahrt.
Rocchini, F., Conti, P., 2014. An improved simulator of AC45 failing catamarans for crew training. In: International Conference on Sport Sciences Research and Technology Support, IcSPORTS.
Savitsky, D., Knowles, P.C., Alaez, J.A., Muller-Graf, B., Murakami, T., van Oossanen, P., Prokhorov, S.D., Rutgersson, O., Wilson, R.A., 1984. Report of the High Speed Marine Vehicle Committee, 17th International Towing Tank Conference. Technical Report, International Towing Tank Conference.
Silverstein, A., 1934. Scale Effect on Clark Y Airfoil Characteristics from NACA Full-Scale Wind-Tunnel Tests. Technical Report, NACA Technical Report No. 502, National Advisory Committee for Aeronautics.
Silverstein, A., Becker, J.V., 1939. Determination of Boundary-Layer Transition on Three Symmetrical Airfoils in the NACA Full-Scale Wind Tunnel. Technical Report, NACA Technical Report No. 637, National Advisory Committee for Aeronautics.
Stack, J., 1931. Tests in the Variable Density Wind Tunnel to Investigate the Effects of Scale and Turbulence on Airfoil Characteristics. Technical Report, NACA Technical Report No. 364, National Advisory Committee for Aeronautics.
Svenneby, E.J., Minsaas, K.J., 1992. Foilcat 2900, design and performance. In: Proceedings of the Third Conference on High-SPeed Marine Craft.
Theodorsen, T., 1935. General Theory of Aerodynamic Instability and the Mechanism of Flutter. Technical Report, NACA Technical Report No. 496, National Advisory Committee of Aeronautics.
Toki, N., Kitajima, Y., Ohnaka, S., Kitamura, T., Yamamoto, I., 1993. Model tests and the development of control system for the super-shuttle 400 "RAINBOW". In: 2nd International Conference on Fast Sea Transportation, FAST.
van Garrel, A., 2003. Development of a Wind Turbine Aerodynamics Simulation Module. Technical Report, Energy research Centre of the Netherlands.
Vernengo, G., Bonfiglio, L., Brizzolara, S., 2017. Supercavitating three-dimensional hydrofoil analysis by viscous lifting-line approach. AIAA J..
Wadlin, K.L., Shuford, C.L.J., McGehee, J.R., 1955. A Theoretical and Experimental Investigation of the Lift and Drag Characteristics of Hydrofoils at Subcritical and Supercritical Speeds. Technical Report, NACA Technical Report No. 1232, National Advisory Committee for Aeronautics.
van Walree, F., 1999. Computational Methods for Hydrofoil Craft in Steady and Unsteady Flow (Ph.D. thesis). Delft University of Technology.
van Walree, F., Buccini, C., Genova, P.A., 1991. The prediction of the hydrodynamic performance of hydrofoil craft in waves. In: 1st International Conference on Fast Sea Transportation, FAST.
Wilson, M.B., 1983. Experimental Determination of Low Froude Number Hydrofoil Performance in Calm Water and in Regular Waves. Technical Report, David W. Taylor Naval Ship Research and Development Center.